

Cite this: *Chem. Sci.*, 2019, 10, 7029

All publication charges for this article have been paid for by the Royal Society of Chemistry

# Thermodynamic and kinetic studies of H<sub>2</sub> and N<sub>2</sub> binding to bimetallic nickel-group 13 complexes and neutron structure of a Ni( $\eta^2$ -H<sub>2</sub>) adduct†

Ryan C. Cammarota,<sup>‡a</sup> Jing Xie,<sup>‡abe</sup> Samantha A. Burgess,<sup>‡c</sup> Matthew V. Vollmer,<sup>a</sup> Konstantinos D. Vogiatzis,<sup>‡abf</sup> Jingyun Ye,<sup>‡ab</sup> John C. Linehan,<sup>‡c</sup> Aaron M. Appel,<sup>‡c</sup> Christina Hoffmann,<sup>‡d</sup> Xiaoping Wang,<sup>‡d</sup> Victor G. Young, Jr.<sup>a</sup> and Connie C. Lu<sup>‡\*a</sup>

Understanding H<sub>2</sub> binding and activation is important in the context of designing transition metal catalysts for many processes, including hydrogenation and the interconversion of H<sub>2</sub> with protons and electrons. This work reports the first thermodynamic and kinetic H<sub>2</sub> binding studies for an isostructural series of first-row metal complexes: NiML, where M = Al (1), Ga (2), and In (3), and L = [N(o-(NCH<sub>2</sub>PiPr<sub>2</sub>)C<sub>6</sub>H<sub>4</sub>)<sub>3</sub>]<sup>3-</sup>. Thermodynamic free energies ( $\Delta G^\circ$ ) and free energies of activation ( $\Delta G^\ddagger$ ) for binding equilibria were obtained via variable-temperature <sup>31</sup>P NMR studies and lineshape analysis. The supporting metal exerts a large influence on the thermodynamic favorability of both H<sub>2</sub> and N<sub>2</sub> binding to Ni, with  $\Delta G^\circ$  values for H<sub>2</sub> binding found to span nearly the entire range of previous reports. The non-classical H<sub>2</sub> adduct, ( $\eta^2$ -H<sub>2</sub>)NiInL (3-H<sub>2</sub>), was structurally characterized by single-crystal neutron diffraction—the first such study for a Ni( $\eta^2$ -H<sub>2</sub>) complex or any d<sup>10</sup> M( $\eta^2$ -H<sub>2</sub>) complex. UV-Vis studies and TD-DFT calculations identified specific electronic structure perturbations of the supporting metal which poise NiML complexes for small-molecule binding. ETS-NOCV calculations indicate that H<sub>2</sub> binding primarily occurs via H–H  $\sigma$ -donation to the Ni 4p<sub>z</sub>-based LUMO, which is proposed to become energetically accessible as the Ni(0) → M(III) dative interaction increases for the larger M(III) ions. Linear free-energy relationships are discussed, with the activation barrier for H<sub>2</sub> binding ( $\Delta G^\ddagger$ ) found to decrease proportionally for more thermodynamically favorable equilibria. The  $\Delta G^\circ$  values for H<sub>2</sub> and N<sub>2</sub> binding to NiML complexes were also found to be more exergonic for the larger M(III) ions.

Received 24th April 2019

Accepted 8th June 2019

DOI: 10.1039/c9sc02018g

rsc.li/chemical-science

## Introduction

Developing homogeneous base metal catalysts which can activate H<sub>2</sub> and selectively mediate catalytic hydrogenation, H<sub>2</sub> oxidation, and proton reduction have been active areas of

research in recent years.<sup>1–5</sup> In such processes, the strength of H<sub>2</sub> binding, the interplay between  $\sigma$ -donation (H<sub>2</sub>  $\sigma \rightarrow M$ ) and  $\pi$ -back-donation (M  $\rightarrow$  H<sub>2</sub>  $\sigma^*$ ), the resulting extent of H–H activation, and the ease of generating reactive M–H species all can play a critical role in determining catalytic activity and selectivity. H<sub>2</sub> activation is typically initiated by side-on binding of H<sub>2</sub> to form a M( $\eta^2$ -H<sub>2</sub>) adduct, which precedes the generation of reactive M–H species via subsequent oxidative addition or deprotonation events.<sup>6–8</sup> Despite the ubiquity of H<sub>2</sub> binding as a key fundamental reaction step in catalysis,<sup>9</sup> limited experimental data has been reported regarding the thermodynamic and kinetic favorability of H<sub>2</sub> binding to transition metals, especially for the first-row transition metals.<sup>6–8</sup> To the best of our knowledge, thermodynamic H<sub>2</sub>-binding data have only been reported for a handful of first-row metal complexes: Cr(PCy<sub>3</sub>)<sub>2</sub>(CO)<sub>3</sub>,<sup>10,11</sup> [Mn(CO)(dppe)<sub>2</sub>]<sup>†</sup>,<sup>12</sup> [Fe(P<sub>4</sub>N<sub>2</sub>)]<sup>†</sup>,<sup>13</sup> and Co(TPB),<sup>14</sup> where dppe is bis(diphenylphosphino)ethane, P<sub>4</sub>N<sub>2</sub> is a tetraphosphine with two pendant amines, and TPB is tris(o-diisopropylphosphinophenyl)borane. Moreover, without a series of similar M( $\eta^2$ -H<sub>2</sub>) adducts with which to compare

<sup>a</sup>Department of Chemistry, University of Minnesota-Twin Cities, 207 Pleasant Street SE, Minneapolis, Minnesota 55455, USA. E-mail: clu@umn.edu

<sup>b</sup>Supercomputing Institute, Chemical Theory Center, University of Minnesota-Twin Cities, 207 Pleasant Street SE, Minneapolis, Minnesota 55455, USA

<sup>c</sup>Catalysis Science Group, Pacific Northwest National Laboratory, P. O. Box 999, MS K2-57, Richland, Washington 99352, USA

<sup>d</sup>Neutron Scattering Division, Oak Ridge National Laboratory, Oak Ridge, Tennessee 37831, USA

<sup>e</sup>Key Laboratory of Cluster Science of Ministry of Education, School of Chemistry and Chemical Engineering, Beijing Institute of Technology, Beijing 100081, China

<sup>f</sup>Department of Chemistry, University of Tennessee, Knoxville, Tennessee 37996, USA

† Electronic supplementary information (ESI) available: Additional data for crystallographic, thermodynamic, kinetic, and computational studies (PDF), DFT-optimized geometries (XYZ), X-ray and neutron crystallographic data for 3-H<sub>2</sub> (CIF). CCDC 1889774 and 1889775. For ESI and crystallographic data in CIF or other electronic format see DOI: 10.1039/c9sc02018g

‡ These authors contributed equally.

thermodynamic data, the understanding gained by quantifying H<sub>2</sub> binding to a single metal complex are relatively limited.

Recently, the double-decker ligand, [N(*o*-(NCH<sub>2</sub>P<sup>i</sup>Pr<sub>2</sub>)C<sub>6</sub>H<sub>4</sub>)<sub>3</sub>]<sup>3−</sup> (abbreviated as L), was used to prepare bimetallic (η<sup>2</sup>-H<sub>2</sub>)M<sub>A</sub>M<sub>B</sub>L complexes in which group 13 Lewis acidic supporting metal ions (M<sub>B</sub>) induce H<sub>2</sub> binding at Ni(0) and Co(−I) metal centers (M<sub>A</sub>).<sup>15,16</sup> Figueroa and Gabbaï have independently shown that appending a Lewis acidic σ-acceptor to a d<sup>10</sup> transition metal induces binding of a Lewis base donor *trans* to the σ-acceptor.<sup>17–19</sup> We and others have used a tethered σ-acceptor to promote activity at the transition metal for catalytic CO<sub>2</sub> functionalization.<sup>20–22</sup> Here, we report the first thermodynamic and kinetic studies of H<sub>2</sub> binding to a Ni center in an isostructural series, where M<sub>B</sub> = Al, Ga, and In. In the case of the In(III) supporting ion, strong H<sub>2</sub> binding allowed for structural elucidation *via* single-crystal neutron diffraction. Significant modulation of the thermodynamic favorability of both H<sub>2</sub> and N<sub>2</sub> binding to Ni was enabled by introducing and varying the group 13 supporting metal ion, with H<sub>2</sub> binding free energies (Δ*G*°) found to span nearly the entire range of previously reported values. The (η<sup>2</sup>-H<sub>2</sub>)NiML complexes also exhibit different extents of H–H activation and kinetic rates of H<sub>2</sub> binding and loss. Through a combination of experimental and theoretical studies on binding and electronic structure, we present a comprehensive understanding of how a supporting group 13 metal ion poises a proximal transition metal for small-molecule binding and influences both the thermodynamics and kinetics of binding equilibria.

## Results & discussion

### Part I. Neutron diffraction study of (η<sup>2</sup>-H<sub>2</sub>)NiInL and NMR characterization of (η<sup>2</sup>-H<sub>2</sub>)NiAlL

We have previously reported a series of bimetallic NiML complexes featuring Ni(0)→M(III) dative bonds (M = Al (1), Ga (2), and In (3)), where larger group 13 ions, Ga and In, promote H<sub>2</sub> binding to formally d<sup>10</sup> Ni centers.<sup>16</sup> The resulting non-classical H<sub>2</sub> adducts, (η<sup>2</sup>-H<sub>2</sub>)NiGaL (2-H<sub>2</sub>) and (η<sup>2</sup>-H<sub>2</sub>)NiInL (3-H<sub>2</sub>), were characterized by <sup>1</sup>H NMR spectroscopy techniques. In addition, the remarkable stability of 3-H<sub>2</sub> allowed for its molecular structure to be determined by single-crystal X-ray diffraction at 123 K.<sup>16</sup> We currently report a single-crystal neutron diffraction study of 3-H<sub>2</sub> at 100 K (Fig. 1) and the corresponding X-ray structure at 100 K. To our knowledge, 3-H<sub>2</sub> is the first H<sub>2</sub> adduct of Ni, or of any d<sup>10</sup> metal, to be structurally characterized by neutron diffraction. To date, only two other Ni(0) H<sub>2</sub>-adducts have been reported, [O(SiH(*o*-<sup>i</sup>Pr<sub>2</sub>PC<sub>6</sub>H<sub>4</sub>)<sub>2</sub>)<sub>2</sub>]Ni<sub>2</sub>(η<sup>2</sup>-H<sub>2</sub>)<sub>2</sub> and [PhB(*o*-<sup>i</sup>Pr<sub>2</sub>PC<sub>6</sub>H<sub>4</sub>)<sub>2</sub>][Ni(η<sup>2</sup>-H<sub>2</sub>)], both of which were characterized *in situ* at low *T*.<sup>23,24</sup>

Table 1 displays selected structural parameters for 3-H<sub>2</sub>. Of note, the bond distances for non-hydrogen atoms in the X-ray and neutron structures of 3-H<sub>2</sub> are essentially identical within experimental error (Table S4†). The Ni–H distances between the two structures are also within error, though the H–H bond length differs by 0.12 Å. The neutron structure, which is more reliable for placement of H atoms, validates an intact H<sub>2</sub> molecule that is bound in side-on fashion to the Ni center. Upon



Fig. 1 Neutron structure of 3-H<sub>2</sub>. Ellipsoids are shown at the 50% probability level, and H atoms (with the exception of H<sub>2</sub>) have been omitted for clarity.

H<sub>2</sub> coordination, the Ni–In bond distance increases slightly from 2.457(1) Å in 3 to 2.4789(2) Å in 3-H<sub>2</sub>. The H–H bond length of 0.80(2) Å is slightly elongated relative to that in free H<sub>2</sub> (0.74 Å), but shorter than the solution-state distance of 0.91 Å that was determined based on the *J*<sub>H<sub>2</sub></sub> coupling constant of 3-HD.<sup>16</sup> This discrepancy can be attributed to rapid librational motion of H<sub>2</sub> in 3-H<sub>2</sub>, a phenomenon which typically leads to an average contraction of ~0.07 Å in the apparent solid-state H–H bond distance relative to the solution-state distance determined by NMR studies.<sup>7,25–27</sup> Consistent with this attribution, fast H<sub>2</sub> rotation in solution relative to molecular tumbling is also supported by the previously reported *T*<sub>1</sub> (min) value for the coordinated H<sub>2</sub> ligand of 3-H<sub>2</sub>.<sup>16</sup>

Notably, the Ni–H bond distance is a parameter that neutron diffraction is uniquely able to experimentally evaluate. The two equivalent Ni–H bond lengths of 1.61(2) Å fall on the longer end of the wide range of the Ni–H distances reported for terminal Ni hydrides (*cf.* 1.32 to 1.65 Å).<sup>28</sup> Although direct comparisons are

Table 1 Selected structural metrics for 3-H<sub>2</sub> from X-ray and neutron studies at 100 K<sup>a</sup>

	3-H <sub>2</sub> (neutron)	3-H <sub>2</sub> (X-ray)
H–H	0.80(2)	0.92(3)
Ni–H	1.61(2)	1.58(2)
	1.61(2)	1.65(2)
Ni–In	2.39(2)	2.4789(2)
Ni–P (avg.)	2.26(1)	2.2618(4)
In–N <sub>amide</sub> (avg.)	2.13(1)	2.115(1)
In–N <sub>apical</sub>	2.40(2)	2.366(1)
Ni to P <sub>3</sub> -plane	0.31	0.29
In to N <sub>3</sub> -plane	0.52	0.50

<sup>a</sup> Values in Å (estimated standard deviations in parentheses). See Table 6 for crystallographic details. See Table S4 for a detailed comparison of the X-ray and neutron structures.



sparse due to the rarity of structurally characterized  $M(\eta^2-H_2)$  complexes, the M–H and H–H distances in **3**- $H_2$  are both similar to those for  $(\eta^2-H_2)Co(TPB)$ , which has M–H and H–H distances of 1.66/1.67 Å and 0.83(2) Å, respectively.<sup>29</sup> Short contact distances between the  $H_2$  unit and the hydrogen atoms of the ligand isopropyl phosphine groups were observed in both **3**- $H_2$  and  $(\eta^2-H_2)Co(TPB)$ , the closest of which were 2.24 Å and 2.10 Å, respectively. These distances are, within error, close to the intermolecular  $H\cdots H$  van der Waals distance (2.2 Å).<sup>30</sup>

Previously, no reaction was observed between  $NiAlL$  (**1**) and  $H_2$  (1 atm) at room temperature. Subsequent studies have found that either high  $H_2$  pressure or low  $T$  is needed to observe  $H_2$  binding to **1**. At 34 atm  $H_2$  and 232 K, a new species was observed by  $^1H$  NMR spectroscopy that is assigned as  $(\eta^2-H_2)NiAlL$  (**1**- $H_2$ ) based on a diagnostic resonance for bound  $H_2$  at  $-1.5$  ppm (Fig. S8 and S9†) and a short  $T_1$  (min) value of  $\leq 49(5)$  ms (500 MHz, THF- $d_8$ ; Fig. S10†).<sup>31,32</sup> The  $^1H$  NMR spectrum of the HD isotopomer,  $(\eta^2-HD)NiAlL$  (**1**-HD), which was formed at 213 K under 3.8 atm HD, displayed a characteristic 1 : 1 : 1 triplet for the bound HD ligand, with  $J_{HD} = 34.4$  Hz (Fig. S11†).

With the addition of **1**- $H_2$  to complete the isostructural trio of  $Ni(\eta^2-H_2)$  complexes, it is apparent that  $H_2$  activation increases as the supporting metal is varied down group 13 from Al to Ga to In, as reflected by the decreasing  $J_{HD}$  values (in Hz): 34.4 for **1**-HD > 33.2 for **2**-HD > 31.7 for **3**-HD (at 213 K; Fig. S11†). Thus, the corresponding estimated solution-state H–H bond distances increase as the supporting metal is varied down group 13, from 0.86 Å for **1**- $H_2$ , to 0.88 Å for **2**- $H_2$ , to 0.91 Å for **3**- $H_2$ .<sup>33</sup> The relative extents of H–H bond activation for the  $(\eta^2-H_2)NiML$  complexes are also in accord with those predicted by DFT calculations (Tables S13, S19 and S20†). That **1**- $H_2$  would have the shortest H–H distance of the trio, and the closest to that of free  $H_2$ , is suggestive of the weak and labile nature of  $H_2$  binding to **1** relative to  $H_2$  binding to **2** and **3**.<sup>6,7</sup> We further note that the isostructural mononuclear Ni complex,  $NiLH_3$  (**4**),<sup>34</sup> does not bind  $H_2$  even under forcing conditions (193 K, 34 atm  $H_2$ ),<sup>20</sup> which suggests that the supporting metal

plays a pivotal role in inducing  $H_2$  binding and controlling the extent of  $H_2$  activation. Lastly, both **2**- $H_2$  and **3**- $H_2$  exhibit a greater extent of  $H_2$  activation compared to the two other  $Ni(0)$   $H_2$ -adducts:  $[O(SiH(o-^iPr_2PC_6H_4)_2)_2]Ni_2(\eta^2-H_2)_2$  ( $J_{HD} = 34.2$  Hz) and  $[PhB(o-^iPr_2PC_6H_4)_2]Ni(\eta^2-H_2)$  ( $J_{HD} = 36.5$  Hz).<sup>23,24</sup>

## Part II. $H_2$ and $N_2$ binding energies for the NiML triad

Intrigued by the varied propensities for binding and activating  $H_2$  enabled by changing a single atom, we set out to understand how the group 13 supporting metal influences the thermodynamics and kinetics of  $Ni-H_2$  binding equilibria. Previously,  $(\eta^2-H_2)NiGaL$  (**2**- $H_2$ ) was generated *in situ* under 1 atm  $H_2$ , but reverted to **2** upon exposure to vacuum or Ar.<sup>16</sup> Because of its reversible  $H_2$  binding at ambient conditions, **2** was an ideal candidate for initiating binding equilibrium studies. Variable-temperature (VT)  $^{31}P$  NMR spectra of **2** in toluene- $d_8$  under 6.8 atm  $H_2$  displayed a single resonance, which shifted downfield from 42.7 to 56.4 ppm as the temperature was decreased from 368 K to 221 K (Fig. 2a). As a control experiment, the VT NMR profile of **2** under Ar showed a minimal change in the  $^{31}P$  shift ( $\Delta\delta < 0.5$  ppm) over a similar  $T$  range (Fig. S12 and S13†). Hence, the VT NMR behavior of **2** under an  $H_2$  atmosphere is consistent with an equilibrium between **2** and **2**- $H_2$  that is governed by fast chemical exchange relative to the  $^{31}P$  NMR timescale (202.4 MHz), where the latter is favored at low  $T$  and both species are three-fold symmetric in solution.

Analogous VT  $^{31}P$  NMR experiments were also performed for **2** under various  $H_2$  pressures of 1.0, 13.6, and 34 atm (Fig. S1, S14 and S15†). Of note, for all  $H_2$  pressures examined, the same low  $T$  convergence of the  $^{31}P$  resonance to  $\sim 56.9$  ppm was observed at 193 K, which corresponds to the  $^{31}P$  chemical shift of **2**- $H_2$  (Fig. 2b). At high  $T$ , the observed  $^{31}P$  chemical shift approaches that of **2**, with closer convergence observed at lower  $H_2$  pressures. These observations are consistent with rapid interconversion between **2** and **2**- $H_2$ , such that the observed chemical shift ( $^{31}P$   $\delta$ ) is the population-weighted average of the chemical shifts of these exchanging species.<sup>35</sup> Thus, the

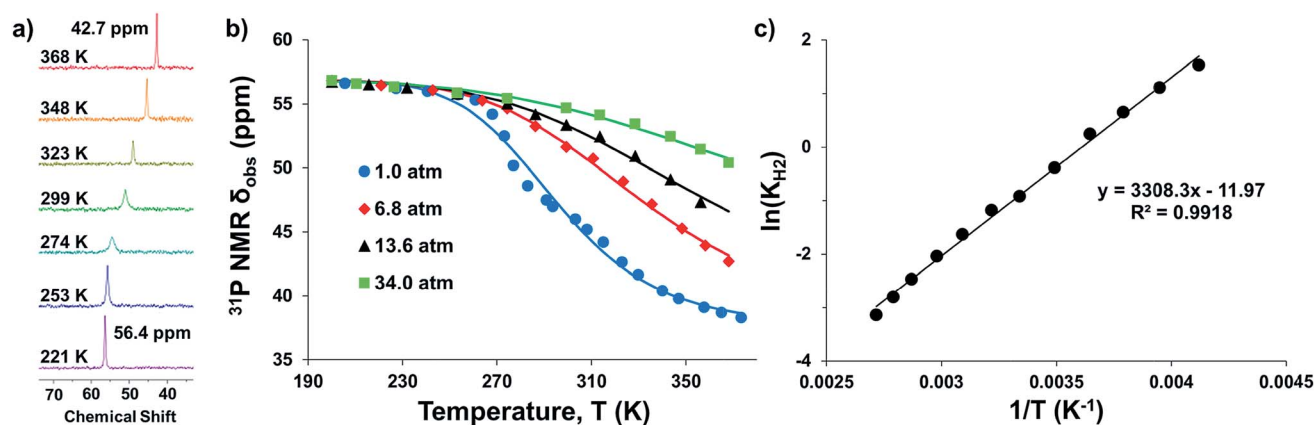


Fig. 2 (a) VT  $^{31}P$  NMR spectra of **2** under 6.8 atm  $H_2$  in toluene- $d_8$  from 368 to 221 K. (b) Plots of  $^{31}P$   $\delta$  vs.  $T$  obtained for various  $H_2$  pressures. Data are shown as points, and solid traces represent the best-fit curves obtained by varying  $\Delta H^\circ$  and  $\Delta S^\circ$  as parameters (see ESI†). (c) Representative van't Hoff plot of  $\ln(K_{H_2})$  vs.  $1/T$  at 6.8 atm  $H_2$ . The thermodynamic binding parameters shown in Table 2 were determined from van't Hoff plots for data sets collected at 6.8 and 13.6 atm  $H_2$ , which exhibit fast chemical exchange.



observed  $^{31}\text{P}$   $\delta$  can be converted into the equilibrium concentration ratio of **2** and **2-H<sub>2</sub>** (see ESI†). The equilibrium constant for  $\text{H}_2$  binding,  $K_{\text{H}_2}$ , was determined according to eqn (1), where  $P_{\text{H}_2}$  is the  $\text{H}_2$  pressure:

$$K_{\text{H}_2} = \frac{[(\eta^2\text{-H}_2)\text{NiML}]}{[\text{NiML}] \times P_{\text{H}_2}} \quad (1)$$

Next, the thermodynamic parameters for  $\text{H}_2$  binding,  $\Delta H^\circ$ ,  $\Delta S^\circ$ , and  $\Delta G^\circ$ , were determined using two complementary methods: (1) non-linear fitting of the  $^{31}\text{P}$   $\delta$  vs.  $T$  plot in Fig. 2b; and (2) linear regression of the van't Hoff plot of  $\ln(K_{\text{H}_2})$  vs.  $1/T$ , as shown in Fig. 2c. The analyses were performed using the 6.8 and 13.6 atm datasets, where chemical exchange was rigorously fast relative to the  $^{31}\text{P}$  NMR timescale and the variability of  $^{31}\text{P}$   $\delta$  with  $T$  was significant enough to reflect the sampling of an adequate portion of the binding equilibrium. The van't Hoff plot gives  $\Delta H^\circ = -6.3(2)$  kcal mol $^{-1}$ ,  $\Delta S^\circ = -23.0(7)$  cal (mol K) $^{-1}$ , and  $\Delta G^\circ = +0.6(3)$  kcal mol $^{-1}$  for  $\text{H}_2$  binding to **2**, where the standard state conditions are defined as 298 K, 1 atm  $\text{H}_2$ , and 1 M concentrations of all other species in toluene- $d_8$ . Non-linear fitting of the  $^{31}\text{P}$   $\delta$  vs.  $T$  plot yields the same thermodynamic values within experimental error (Fig. S16, S17 and Table S2†).

The  $\text{H}_2$  binding equilibria for the other NiML complexes, **1** ( $M = \text{Al}$ ) and **3** ( $M = \text{In}$ ), were also investigated by VT  $^{31}\text{P}$  NMR spectroscopy. For  $\text{H}_2$  binding to **1**, the VT  $^{31}\text{P}$  NMR spectra in toluene- $d_8$  (363 to 210 K, 34 atm  $\text{H}_2$ ) show a single  $^{31}\text{P}$  resonance shifting downfield relative to that of **1** (30.7 ppm) with decreasing  $T$ , and ultimately converging to a chemical shift of  $\sim 44.3$  ppm for **1-H<sub>2</sub>** (Fig. S18†). The corresponding van't Hoff analysis for  $\text{H}_2$  binding to **1** gives  $\Delta H^\circ = -6.3(1)$  kcal mol $^{-1}$ ,  $\Delta S^\circ = -26.4(4)$  cal (mol K) $^{-1}$ , and  $\Delta G^\circ = +1.6(2)$  kcal mol $^{-1}$  (Fig. S19†). Since **3** binds  $\text{H}_2$  strongly, sub-ambient  $\text{H}_2$  pressure was necessary to establish a measurable equilibrium between **3** and **3-H<sub>2</sub>** (Fig. S20–S22†). Under 1 atm of 10%  $\text{H}_2$  in Ar, where  $P_{\text{H}_2} = 0.1$  atm, a single  $^{31}\text{P}$  peak was observed from 299 to 357 K (Fig. S20†). However, the lineshapes of the observed  $^{31}\text{P}$  peaks are noticeably broadened, which indicates that chemical

exchange between **3** and **3-H<sub>2</sub>** falls into the fast-intermediate regime relative to the  $^{31}\text{P}$  NMR timescale.<sup>36</sup> This is problematic because non-Lorentzian lineshapes and exchange broadening may diminish the reliability of the thermodynamic parameters determined under fast-intermediate exchange conditions.<sup>37</sup> Hence, we caution that the thermodynamic values for  $\text{H}_2$  binding to **3**,  $\Delta H^\circ = -14.8(6)$  kcal mol $^{-1}$ ,  $\Delta S^\circ = -37(2)$  cal mol $^{-1}$  K $^{-1}$ , and  $\Delta G^\circ = -3.7(7)$  kcal mol $^{-1}$  (Fig. S23† and Table 2), should be treated as estimates.

To assess the reliability of this estimated  $\Delta G^\circ$  value, a control experiment was performed on **2** under identical conditions with 0.1 atm  $\text{H}_2$ , which showed similarly broad  $^{31}\text{P}$  peaks due to fast-intermediate chemical exchange (Fig. S24 and S25†). Comparing the binding parameters obtained for **2** under 0.1 atm  $\text{H}_2$  to those obtained under rigorously fast exchange conditions (6.8 and 13.6 atm  $\text{H}_2$ ), we find that the thermodynamic favorability of  $\text{H}_2$  binding was overestimated by 0.7 kcal mol $^{-1}$  using the 0.1 atm  $\text{H}_2$  dataset. Thus, by applying this 0.7 kcal mol $^{-1}$  empirical correction, we propose that a better  $\Delta G^\circ$  estimate for  $\text{H}_2$  binding to **3** is  $-3.0(7)$  kcal mol $^{-1}$ . In support, lineshape simulations of VT  $^{31}\text{P}$  NMR spectra of **3** under 1 atm  $\text{H}_2$  independently gives  $\Delta G^\circ = -2.3(2)$  kcal mol $^{-1}$ , which is within experimental error of the corrected value of  $-3.0(7)$  kcal mol $^{-1}$  (Fig. S26†).

Next, we sought to investigate the related equilibria of  $\text{N}_2$  binding to the NiML complexes using VT  $^{31}\text{P}$  NMR experiments. The equilibrium between **2** and **2-N<sub>2</sub>** was monitored at 1 atm  $\text{N}_2$  and low  $T$  (226 to 193 K). Distinct  $^{31}\text{P}$  resonances were observed for both **2** and **2-N<sub>2</sub>** (Fig. S30†), which is characteristic of slow chemical exchange relative to the  $^{31}\text{P}$  NMR timescale (161.9 MHz). Quantitative integration of the  $^{31}\text{P}$  NMR peaks for **2** and **2-N<sub>2</sub>** allowed for a straightforward determination of  $K_{\text{N}_2}$  using eqn (2), where  $P_{\text{N}_2}$  is the  $\text{N}_2$  pressure:

$$K_{\text{N}_2} = \frac{[(\text{N}_2)\text{NiML}]}{[\text{NiML}] \times P_{\text{N}_2}} \quad (2)$$

Conversely, the interconversion of **3** and **3-N<sub>2</sub>** is fast relative to the  $^{31}\text{P}$  NMR timescale (161.9 MHz) at 1 atm  $\text{N}_2$  and  $T > 288$  K (Fig. S6 and S31†). As such, the observed chemical shift of the single  $^{31}\text{P}$  NMR resonance represents the population-weighted average of the chemical shifts of **3** and **3-N<sub>2</sub>**, and the VT NMR data were analyzed as previously described for  $\text{H}_2$  binding to **2** (Fig. S31 and S32†). Lastly, the observed equilibrium between **1** and **1-N<sub>2</sub>** at 51 atm  $\text{N}_2$  switches from slow exchange at low  $T$  ( $\leq 210$  K) to fast exchange at higher  $T$  ( $\geq 243$  K) (Fig. S33†). Thus,  $K_{\text{N}_2}$  was evaluated based on the distinct  $^{31}\text{P}$  NMR peak integrations for **1** and **1-N<sub>2</sub>** at low  $T$ , and based on the observed  $^{31}\text{P}$  chemical shift at high  $T$ . The thermodynamic binding parameters for the  $\text{H}_2$  and  $\text{N}_2$  binding equilibria of the NiML complexes are compiled in Tables 2 and 3. Additionally, DFT calculations using the M06-L<sup>38</sup>/bs1 method correctly predict the experimental trends in both the  $\text{H}_2$  and  $\text{N}_2$  binding free energies for the trio of NiML complexes (Tables 2 and 3).

Across the NiML series,  $\Delta G^\circ$  for both  $\text{H}_2$  and  $\text{N}_2$  binding was modulated by  $\sim 5$  kcal mol $^{-1}$ , with increasing thermodynamic favorability for both  $\text{H}_2$  and  $\text{N}_2$  binding observed as the

**Table 2** Experimental and DFT-calculated  $\text{H}_2$  thermodynamic binding parameters for **1**, **2**, and **3**<sup>a</sup>

	<b>1</b>	<b>2</b> <sup>b</sup>	<b>3</b>
$\Delta H^\circ$ (kcal mol $^{-1}$ )	−6.3(1)	−6.3(2)	−14.8(6) <sup>d</sup>
$\Delta S^\circ$ (cal mol $^{-1}$ K $^{-1}$ )	−26.4(4)	−23.0(7)	−37(2) <sup>d</sup>
$\Delta G^\circ$ (kcal mol $^{-1}$ )	1.6(2)	0.6(3)	−3.7(7) <sup>d</sup> −3.0(7) <sup>e</sup>
$\Delta G^\circ$ (DFT) <sup>c</sup>	2.8	0.9	−1.9

<sup>a</sup> Standard deviations obtained from van't Hoff linear regression analyses are given in parentheses. Standard state is defined as 298 K, 1 atm  $\text{H}_2$  (or  $\text{N}_2$ ), and 1 M of all other species in toluene- $d_8$ . <sup>b</sup>  $\text{H}_2$  binding studies have also been conducted for **2** in THF (Fig. S27–S29):  $\Delta G^\circ = +0.1(1)$  kcal mol $^{-1}$ ,  $\Delta H^\circ = -7.5(1)$  kcal mol $^{-1}$ , and  $\Delta S^\circ = -25.4(1)$  cal mol $^{-1}$  K $^{-1}$ . <sup>c</sup> Units of kcal mol $^{-1}$ , see Computational methods in Experimental section for details. <sup>d</sup> Estimated values extracted from fast-intermediate exchange regime data (Fig. S20–S23). <sup>e</sup> Corrected  $\Delta G^\circ$  value of  $-3.0(7)$  kcal mol $^{-1}$  is likely a better estimate. See text for explanation of the  $+0.7$  kcal mol $^{-1}$  correction term.





**Table 3** Experimental and DFT-calculated N<sub>2</sub> thermodynamic binding parameters for **1**, **2**, and **3**<sup>a</sup>

	<b>1</b>	<b>2</b>	<b>3</b>
$\Delta H^\circ$ (kcal mol <sup>-1</sup> )	-4.7(2)	-4.7(3)	-14.5(3)
$\Delta S^\circ$ (cal mol <sup>-1</sup> K <sup>-1</sup> )	-27.5(5)	-23(1)	-45(1)
$\Delta G^\circ$ (kcal mol <sup>-1</sup> )	3.5(3)	2.1(5)	-1.2(4)
$\Delta G^\circ$ (DFT) <sup>b</sup>	6.3	3.6	0.2

<sup>a</sup> Same as Table 2 footnote *a*. <sup>b</sup> Same as Table 2 footnote *c*.

supporting metal was varied down group 13 (Tables 2 and 3). Notably,  $\Delta G^\circ$  values for H<sub>2</sub> binding to the NiML complexes nearly span the entire range of previously reported values (from -2 to +3 kcal mol; Tables S6 and S7†). This is remarkable considering that the full range of literature  $\Delta G^\circ$  values encompasses H<sub>2</sub> binding to various transition metals (*e.g.* Cr, Mo, W, Re, Fe, Ru, Co, and Ir) in diverse ligand environments.<sup>10,11,13,14,39–45</sup> In contrast, the NiML trio features an isostructural Ni site within the same ligand framework, where the primary difference is the identity of the group 13 metal. We hypothesize that the strength of the Ni(0)→M(III) dative interaction directly tunes the binding at Ni in the position *trans* to M(III), where greater Ni(0)→M(III) interactions lead to stronger small-molecule binding. This hypothesis is generally consistent with other literature examples wherein the interaction of a  $\sigma$ -acceptor with a d<sup>10</sup> transition metal enhances donor-binding at the *trans* position.<sup>17–19</sup> DFT calculations predict that supporting Ni with In(III) in **3** increases the favorability of H<sub>2</sub> binding by ~8 kcal mol<sup>-1</sup> relative to NiLH<sub>3</sub> (**4**), which are the two limiting extremes in this series (Table S16†).

To the best of our knowledge, ( $\eta^2$ -H<sub>2</sub>)Co(TPB) and [( $\eta^2$ -H<sub>2</sub>)Re(CN<sup>t</sup>Bu)<sub>3</sub>(PCy<sub>3</sub>)<sub>2</sub>]<sup>+</sup> were previously reported to have the most favorable H<sub>2</sub> binding free energies, with  $\Delta G^\circ_{1M} = -4.8(9)$  and  $-4.8(1.3)$  kcal mol<sup>-1</sup>, respectively (Table S7†).<sup>14,39</sup> Notably, **3** binds H<sub>2</sub> even more favorably, with  $\Delta G^\circ_{1M} \sim -6.5(7)$  kcal mol<sup>-1</sup>, which was obtained by converting  $\Delta G^\circ$  at  $P_{H_2} = 1$  atm to  $\Delta G^\circ$  for [H<sub>2</sub>] = 1 M. In addition, the determination of both H<sub>2</sub> and N<sub>2</sub> binding energies for first-row transition metal complexes is rare.<sup>10,11,13,14,46</sup> Across the NiML series, the binding free energies for H<sub>2</sub> are more favorable than those for N<sub>2</sub> by 1.9(4), 1.5(5), and ~1.8(8) kcal mol<sup>-1</sup> for **1**, **2**, and **3**, respectively (Tables 2 and 3). A similar trend was reported for [Fe(P<sub>4</sub>N<sub>2</sub>)]<sup>+</sup> and Cr(CO)<sub>3</sub>(PCy<sub>3</sub>)<sub>2</sub>, whereas  $\Delta G^\circ_{1M}$  energies for H<sub>2</sub> and N<sub>2</sub> binding to Co(TPB) are identical within error (Tables S6–S9†). The finding that N<sub>2</sub> binding is more competitive with H<sub>2</sub> binding for Co(TPB) than it is for NiML complexes is consistent with the greater  $\pi$ -basicity of low-valent Co toward N<sub>2</sub>.<sup>47,48</sup>

In further examining the  $\Delta H^\circ$  and  $\Delta S^\circ$  contributions for binding to NiML (**1–3**), the large negative  $\Delta S^\circ$  values for H<sub>2</sub> and N<sub>2</sub> binding reflect the entropic cost of binding a gas molecule (Tables 2 and 3). In general, a greater entropic cost was observed for N<sub>2</sub> binding than for H<sub>2</sub> binding; this trend can be explained in part by the larger absolute entropy of N<sub>2</sub> relative to H<sub>2</sub>.<sup>11</sup> It is also striking that both H<sub>2</sub> and N<sub>2</sub> binding to **3** are considerably more exothermic ( $\Delta\Delta H^\circ \approx -9$  kcal mol<sup>-1</sup>) and entropically

costly ( $\Delta\Delta S^\circ \approx -13$  and  $-20$  cal mol<sup>-1</sup> K<sup>-1</sup>, respectively) compared with binding to **1** and **2** (Tables 2 and 3). The fact that binding to **3** has the most favorable enthalpic and most unfavorable entropic terms is consistent with tighter and more rigid binding of both H<sub>2</sub> and N<sub>2</sub>. Intriguingly, because **1** and **2** have identical  $\Delta H^\circ$  values for both H<sub>2</sub> and N<sub>2</sub> binding, the differences in their observed binding propensities originate from the differences in  $\Delta S^\circ$  values.

### Part III. Kinetics of self-exchange for NiML and ( $\eta^2$ -H<sub>2</sub>)NiML complexes

To understand the dependence of the kinetics of the H<sub>2</sub> binding process on the supporting metal, VT <sup>31</sup>P NMR lineshape simulations of NiML under 1 atm H<sub>2</sub> were performed to extract self-exchange rates for the interconversion between NiML and ( $\eta^2$ -H<sub>2</sub>)NiML. Exchange rates were determined *via* least-squares fitting of the VT <sup>31</sup>P NMR spectra using a two-site, non-mutual exchange model (see Experimental section and ESI† for details).<sup>49,50</sup> Good agreement was generally achieved between the experimental and simulated spectra, as illustrated in Fig. 3a for the VT <sup>31</sup>P NMR study of **1** under 1 atm H<sub>2</sub>. Similar lineshape analyses were performed for each NiML complex, which allowed exchange rates to be determined at seven or more different temperatures between 213 K and 344 K (Fig. S42–S44†). Notably, the exchange rate decreases by a factor of ~6 at 298 K upon varying the supporting metal from Al to In (Table 4). Exchange rates at 298 K were found to correlate strongly with both H<sub>2</sub> binding free energies ( $R^2 = 0.996$ , Fig. S47†) and H–H bond distances in ( $\eta^2$ -H<sub>2</sub>)NiML complexes ( $R^2 = 0.958$ , Fig. S48†), with slower kinetic rates of H<sub>2</sub> exchange for more thermodynamically favorable binding equilibria where H<sub>2</sub> is more activated. The H<sub>2</sub> binding equilibrium for complex **1** is especially dynamic, with interconversion between **1** and **1**-H<sub>2</sub> occurring over 28 000 times per second at 298 K and 1 atm H<sub>2</sub> (Fig. 3a and Table 4).

We propose a self-exchange mechanism comprised of H<sub>2</sub> loss from ( $\eta^2$ -H<sub>2</sub>)NiML to generate NiML and free H<sub>2</sub>, and H<sub>2</sub> binding to another NiML complex to form ( $\eta^2$ -H<sub>2</sub>)NiML (Fig. 3c). The rate constants for H<sub>2</sub> loss from ( $\eta^2$ -H<sub>2</sub>)NiML,  $k_{\text{loss}}$ , were determined at each *T* based on the exchange rates and the known equilibrium concentrations of ( $\eta^2$ -H<sub>2</sub>)NiML (see ESI†). Eyring analyses for  $k_{\text{loss}}$  allowed for the determination of activation barriers for H<sub>2</sub> loss from ( $\eta^2$ -H<sub>2</sub>)NiML complexes, as shown in Fig. 3b for **1**-H<sub>2</sub>. Eyring plots for H<sub>2</sub> loss from **2**-H<sub>2</sub> and **3**-H<sub>2</sub> are shown in Fig. S49 and S50,† respectively. The free energy barriers for H<sub>2</sub> loss ( $\Delta G^\ddagger_{\text{loss}}$ ) were found to be similar for all complexes (9.1 to 9.4 kcal mol<sup>-1</sup>), with  $\Delta H^\ddagger$  and  $\Delta S^\ddagger$  values ranging from 9.3 to 11.3 kcal mol<sup>-1</sup> and from -0.3 to +7.5 cal (mol K)<sup>-1</sup>, respectively (Table 4). The fact that  $\Delta S^\ddagger_{\text{loss}}$  values are positive or close to zero in all cases is consistent with the expected gain in H<sub>2</sub> freedom of motion, while positive  $\Delta H^\ddagger_{\text{loss}}$  values suggest that partial Ni–H<sub>2</sub> bond breaking is the dominant process involved in reaching the transition state for H<sub>2</sub> loss. Interestingly, both  $\Delta H^\ddagger_{\text{loss}}$  and  $\Delta S^\ddagger_{\text{loss}}$  values for the ( $\eta^2$ -H<sub>2</sub>)NiML complexes decrease as the supporting metal is varied down group 13 (Al > Ga > In; Table 4).





Fig. 3 (a) Selected VT  $^{31}\text{P}$  NMR spectra of **1** under 1 atm  $\text{H}_2$  from 215 to 298 K (red lines, toluene- $d_8$ , 162 MHz) and corresponding simulated spectra (black lines), which were utilized to extract exchange rates at each  $T$  (standard deviations in parentheses). (b) Eyring plot of  $\ln(k_{\text{loss}}/T)$  vs.  $1/T$ , where  $k_{\text{loss}}$  is the first-order rate constant for  $\text{H}_2$  loss from **1**- $\text{H}_2$ . (c) Proposed reaction coordinate diagram for chemical exchange between  $(\eta^2\text{-H}_2)\text{NiML}$  and  $\text{NiML}$  via unimolecular  $\text{H}_2$  loss.

Table 4 Comparison of thermodynamic and kinetic binding parameters for  $\text{H}_2$  self-exchange, binding, and loss for  $\text{NiML}$  complexes (**1**–**3**)<sup>a</sup>

Complex		1	2	3
Self-exchange <sup>b</sup>	Rate <sub>ex</sub> ( $\times 10^4$ )	2.82(3)	2.2(2)	0.437(5)
	Rate <sub>rel</sub>	6.4	4.9	1.0
$\text{H}_2$ loss <sup>c</sup>	$k_{\text{loss}}$ ( $\times 10^6$ )	55(3)	6.5(5)	0.60(3)
	$\Delta H_{\text{loss}}^\ddagger$	11.3(2)	10.1(4)	9.3(4)
	$\Delta S_{\text{loss}}^\ddagger$	7.5(1)	3.5(1)	−0.3(1)
	$\Delta G_{\text{loss}}^\ddagger$	9.1(2)	9.1(4)	9.4(4)
$\text{H}_2$ binding	$\Delta G_{\text{M}}^\ddagger$ <sup>d</sup>	−1.9(2)	−2.9(2)	−6.5(7)
	$\Delta G_{\text{bind}}^\ddagger$	7.2(3)	6.2(5)	2.9(8)

<sup>a</sup> All values determined for a standard state of 1 M  $\text{H}_2$ , 1 M for all other species in toluene- $d_8$ , and 298 K.  $\Delta G_{\text{M}}^\ddagger$ ,  $\Delta G_{\text{loss}}^\ddagger$ , and  $\Delta H_{\text{loss}}^\ddagger$  values are in units of kcal mol<sup>−1</sup>, and  $\Delta S_{\text{loss}}^\ddagger$  values are in units of cal (mol K)<sup>−1</sup>. Rate<sub>ex</sub> and  $k_{\text{loss}}$  are in s<sup>−1</sup>, and rate<sub>rel</sub> is the relative rate. <sup>b</sup>  $[\text{Ni}]_{\text{total}} = 7.5$  mM. <sup>c</sup>  $\Delta G_{\text{loss}}^\ddagger \approx \Delta G_{\text{exchange}}^\ddagger$  for unimolecular  $\text{H}_2$  loss. <sup>d</sup>  $\Delta G_{\text{M}}^\ddagger$  are directly derived from values in Table 2 by converting the standard state for  $\text{H}_2$  from 1 atm  $\text{H}_2$  to 1 M. See ESI for details.

Furthermore,  $\Delta S_{\text{loss}}^\ddagger$  values ( $\sim 0$  or  $>0$ ) are consistent with unimolecular  $\text{H}_2$  loss from  $(\eta^2\text{-H}_2)\text{NiML}$ , as opposed to  $\text{H}_2$  self-exchange *via* an intermolecular  $\text{LMNi}\cdots\text{H}_2\cdots\text{NiML}$  transition state. Such a transition state also seems unlikely because of the steric clash between the diisopropyl ligand groups surrounding each Ni site. Using the proposed reaction coordinate diagram, one can further extract the free energy barrier for  $\text{H}_2$  binding ( $\Delta G_{\text{bind}}^\ddagger$ ) by using the thermodynamic relationship:  $\Delta G_{\text{loss}}^\ddagger = \Delta G_{\text{bind}}^\ddagger - \Delta G_{\text{M}}^\ddagger$ . Of note,  $\Delta G_{\text{M}}^\ddagger$  is the free energy of  $\text{H}_2$  binding after converting the  $\text{H}_2$  standard state from 1 atm (as given in Table 2) to 1 M. Hence, the  $\Delta G_{\text{bind}}^\ddagger$  values for **1**, **2**, and **3** are 7.2(3), 6.2(5), and  $\sim 2.9$ (8) kcal mol<sup>−1</sup>, respectively, where the activation barriers for  $\text{H}_2$  binding are lower for more thermodynamically favorable binding equilibria (Table 4).

Activation barriers and rate constants for  $\text{H}_2$  binding and loss have seldom been reported despite their relevance for

many catalytic processes.  $\Delta H_{\text{loss}}^\ddagger$  values for  $(\eta^2\text{-H}_2)\text{NiML}$  (9.3 to 11.3 kcal mol<sup>−1</sup>) are comparable to those reported (in kcal mol<sup>−1</sup>) for  $[\text{Ru}(\eta^2\text{-H}_2)\text{H}_3(\text{PPh}_3)_3]^+$  (8.8),<sup>31</sup>  $\text{Cr}(\eta^2\text{-H}_2)(\text{CO})_3(\text{PCy}_3)_2$  (12.1),<sup>10</sup>  $\text{Ir}(\eta^2\text{-H}_2)(\text{H})_2\text{X}(\text{P}^t\text{Bu}_2\text{Me})_2$  (9.4 to 11.3 for X = Cl, Br, I),<sup>40</sup> and  $\text{Ir}(\eta^2\text{-H}_2)(\text{H})_2\text{X}(\text{P}^i\text{Pr}_3)_2$  (10.1 to 11.4 for X = Cl, Br, I),<sup>51</sup> and are significantly lower than those reported for  $\text{W}(\eta^2\text{-H}_2)(\text{CO})_3(\text{PCy}_3)_2$  (16.9)<sup>44</sup> and  $\text{Ru}(\eta^2\text{-H}_2)(\text{H})_2(\text{PPh}_3)_3$  (17.9).<sup>31</sup> Perhaps the most thoroughly studied  $\text{H}_2$  binding equilibrium is that of  $\text{W}(\eta^2\text{-H}_2)(\text{CO})_3(\text{PCy}_3)_2$ , for which rate constants for both  $\text{H}_2$  binding ( $k_{\text{bind}}$ ) and loss ( $k_{\text{loss}}$ ) have been directly measured to be  $\sim 2 \times 10^6$  M<sup>−1</sup> s<sup>−1</sup> and 469 s<sup>−1</sup> at 298 K, respectively.<sup>44,52</sup> In comparison, the  $k_{\text{loss}}$  values for  $(\eta^2\text{-H}_2)\text{NiML}$  complexes are 3 to 5 orders of magnitude greater than that for  $\text{W}(\eta^2\text{-H}_2)(\text{CO})_3(\text{PCy}_3)_2$  (Table 4). This can be rationalized by the fact that  $\text{H}_2$  is much more activated in  $\text{W}(\eta^2\text{-H}_2)(\text{CO})_3(\text{PCy}_3)_2$ , which co-exists with its dihydride species at 298 K ( $K \sim 0.25$ ).<sup>7,44,45</sup> In contrast,  $\text{HNi}(\mu\text{-H})\text{ML}$  dihydride species, which have some precedent in the literature,<sup>24,53,54</sup> have not been observed.<sup>16,55</sup> DFT calculations predict such a species to be unstable relative to  $(\eta^2\text{-H}_2)\text{NiML}$  by 12 to 19 kcal mol<sup>−1</sup> under 1 atm  $\text{H}_2$  (Table S25, S26 and Fig. S55†).

#### Part IV. Insights from quantum chemical calculations and UV-Vis spectra

Complexes **1**–**3** and  $\text{NiLH}_3$  (**4**), as well as their  $\text{H}_2$  and  $\text{N}_2$  adducts, were investigated by density functional theory (DFT) calculations using several different functionals and basis sets (see Experimental section and Table S3†). The M06-D3<sup>56,57</sup>/bs4 method gave the best agreement between the optimized and experimental geometries for the three Ni–In complexes: **3**, **3**- $\text{N}_2$ , and **3**- $\text{H}_2$  (Tables S13–S15†).<sup>16</sup> On the other hand, the relative free energies ( $\Delta G^\circ$ ) for  $\text{H}_2$  and  $\text{N}_2$  binding to **1**–**3** were best matched by M06-L<sup>38</sup>/bs1 (Tables S16 and S17†), which correctly predicted the trends of stronger  $\text{H}_2$  binding than  $\text{N}_2$  and increasing binding favorability for  $\text{M} = \text{In} > \text{Ga} > \text{Al}$  (Tables 2 and 3).



To better understand chemical bonding between  $H_2$  and Ni in the  $(\eta^2-H_2)NiML$  complexes, we conducted energy decomposition analysis (EDA).<sup>58</sup> EDA allows for the total interaction energy ( $\Delta E_{int}$ ) between the  $H_2$  and NiML fragments to be partitioned into the following terms: electrostatic energy ( $\Delta E_{elstat}$ ), Pauli repulsive interaction ( $\Delta E_{Pauli}$ ), dispersion ( $\Delta E_{disp}$ ), and covalent interaction ( $\Delta E_{orb}$ ).<sup>58</sup> The  $\Delta E_{orb}$  term can be further divided into individual energy contributions associated with specific orbital interactions, and thereby allows for differentiation of  $\sigma$ ,  $\pi$ , and  $\delta$  bonding interactions. The extended transition-state method coupled with natural orbitals for chemical valence theory (ETS-NOCV<sup>59</sup>) was then utilized to analyze the bonding interactions between Ni and  $H_2$ . Fig. 4 illustrates the two most important NOCV pairs for the Ni- $H_2$  interaction in  $3-H_2$ , in which chemical bonding is indicated by deformation in the electron densities ( $\Delta\rho$ ). Overall, two orbital interactions are important: (1)  $\sigma$ -donation from the  $H_2$   $\sigma$ -bond to the empty Ni  $4p_z$  orbital, which accounts for 56% of  $\Delta E_{orb}$  and is comprised of  $\Delta\rho_1$  (38%; Fig. 4) and  $\Delta\rho_3$  (18%; Fig. S53†); and (2)  $\pi$ -back-donation from a Ni  $3d_\pi$  orbital to the empty  $H_2$   $\sigma^*$  orbital, which accounts for 35% of  $\Delta E_{orb}$ . Similarly, greater contributions of  $\sigma$ -donation (57–59% of  $\Delta E_{orb}$ ) compared to  $\pi$ -back-donation (34–35% of  $\Delta E_{orb}$ ) were also observed for Ni- $H_2$  orbital interactions in  $1-H_2$  and  $2-H_2$  (Table S22†).

The total interaction energy ( $\Delta E_{int}$ ) between the  $H_2$  and Ni fragments becomes increasingly favorable in the order,  $(\eta^2-H_2)NiLH_3 < 1-H_2 < 2-H_2 < 3-H_2$  (Table S21†). Of interest, the less favorable  $\Delta E_{int}$  predicted for  $(\eta^2-H_2)NiLH_3$  arises from a large, unfavorable  $\Delta E_{Pauli}$  term, which is the repulsive interaction energy between like spins in the  $H_2$  and  $NiLH_3$  fragments. This makes sense as  $NiLH_3$  lacks a Ni  $\rightarrow$  M interaction that would result in attenuation of Ni electron density. Within the  $(\eta^2-H_2)NiML$  series, both the  $\Delta E_{elstat}$  and  $\Delta E_{orb}$  terms become more favorable as M is varied down the group 13 triad (Table S21†). Furthermore, the greater relative importance of  $\sigma$ -donation to  $H_2$  binding than  $\pi$ -back-donation is consistent with the trend that  $H_2$  binding favorability increases as the Ni center becomes

more electron-deficient, as judged by the Ni(I/0) redox potentials (Fig. S71 and Table S39†).<sup>16</sup> Hence, we propose that increased electron-withdrawal *via* Ni  $\rightarrow$  M dative bonding as M is varied down group 13 induces stronger electrostatic and covalent interactions between  $H_2$  and NiML, with a concomitant decrease in unfavorable Pauli repulsion between the two fragments.

Given the rarity of  $H_2$  and  $N_2$  binding to a Ni(0) metal center, we next sought to understand the specific electronic perturbations of the supporting group 13 metal ion that poise NiML to bind small molecules. To lend insight, UV-Vis spectroscopy studies in conjunction with time-dependent density functional theory (TD-DFT) calculations were conducted to investigate the electronic structure of complexes **1–4** and their  $H_2$  and  $N_2$  adducts. The UV-Vis spectra of  $NiLH_3$  and **1–3** are shown in Fig. 5a (THF, 298 K), along with the corresponding TD-DFT predicted spectra, where M06-D3/bs4 showed the best agreement with experiment (Fig. 5b and Table S29†). We also sought to understand how the binding of  $H_2$  and  $N_2$  to the NiML complexes further impacts electronic structure. In this regard, it is notable that small-molecule binding to NiML often manifests in vibrant color changes. For example, exposure of a THF solution of **3** under Ar to an  $N_2$  or  $H_2$  atmosphere resulted in a color change from a deep red-purple color to a lighter red ( $3-N_2$ ) or yellow-brown ( $3-H_2$ ), respectively (Fig. 5c).

The UV-Vis spectra of **1–3** share the same pattern of three peaks between 400 and 800 nm, which are marked with asterisks in Fig. 5a and listed in Table 5 as peaks I, II, and III. These peaks all red-shift upon varying the supporting metal from Al to Ga to In. The TD-DFT calculated transition energies for **1–3** agree reasonably well with experiment, with the predicted excitations generally blue-shifted by 0.04 to 0.3 eV for peaks I to III (Table 5). The TD-DFT results also correctly predicted the red-shift of all peaks for **2** relative to **1**, but the subtle spectral differences between **2** and **3** were not discerned by TD-DFT despite testing several methods (Table S29, Fig. S57 and S58†). For  $NiLH_3$ , a broad absorption feature is observed at  $\sim 500$  nm, which was fit with two overlapping peaks with maxima at 491 and 533 nm, along with a low-intensity shoulder at 663 nm (Table S27, Fig. S56†).

UV-Vis peaks I–III for  $NiLH_3$  and **1–3** were assigned based on the TD-DFT results (Table 5). Each peak corresponds to an electronic excitation from either a Ni 3d orbital or a ligand-based molecular orbital (MO) to the lowest unoccupied molecular orbital (LUMO), the latter of which is highly similar for all complexes. For  $NiLH_3$ , the LUMO has both Ni  $4p_z$  and P 4p character, whereas the LUMO for complexes **1–3** also has additional contributions from Ni (3d, 4s) and M (s,  $p_z$ ) atomic orbitals (Fig. S59 and Table S31†). For all complexes, peaks I and II arise from electronic excitations to the LUMO from the Ni  $d_{xy}/d_{x^2-y^2}$  and  $d_{xz}/d_{yz}$  orbitals, respectively. Peak III for  $NiLH_3$  is a transition from a pure  $d_{z^2}$  orbital to the LUMO, while peak III for **1–3** is a more complex transition from a mixed ligand-based arene  $\pi^*$  MO with partial Ni  $d_{z^2}$  character to the LUMO (Table S28†).

Based on these transition assignments, semi-quantitative MO diagrams for  $NiLH_3$  and **1–3** can be constructed (Fig. 6).



Fig. 4 The two dominant NOCV pairs in  $3-H_2$  and their associated deformation densities ( $\Delta\rho_1$ , top right;  $\Delta\rho_2$ , bottom right; contour iso-value = 0.04 a.u.). The colors of the deformation densities indicate the flow of electrons, from red to blue, involved in the Ni- $H_2$  interaction.







**Fig. 5** (a) UV-Vis spectra of  $\text{NiLH}_3$  (grey), **1** (red), **2** (blue), and **3** (black) obtained in THF at room temperature. Inset is a close-up of the 600–800 nm range. (b) TD-DFT predicted spectra of  $\text{NiLH}_3$  and **1–3** (M06-D3/bs4, SMD/THF) shown as dotted lines. (c) UV-Vis spectra of **3** (under Ar, black), **3-N<sub>2</sub>** (under 1 atm N<sub>2</sub>, pink), and **3-H<sub>2</sub>** (under 1 atm H<sub>2</sub>, cyan) in THF at 298 K, with TD-DFT plots shown in the inset. Note that small features corresponding to **3** can be seen in the UV-Vis spectrum of **3-N<sub>2</sub>** due to the equilibrium binding of N<sub>2</sub> under these conditions. Asterisks in spectra correspond to bands I, II, or III, as listed in Table 5.

**Table 5** UV-Vis peaks (nm) for  $\text{NiLH}_3$  and **1–3**, with TD-DFT data (in parentheses) and transition assignments

Peak	Transition	$\text{NiLH}_3$	<b>1</b>	<b>2</b>	<b>3</b>
I	$d_{xy}/d_{x^2-y^2} \rightarrow \text{LUMO}$	663 (490)	600 (573)	638 (650)	699 (642)
II	$d_{yz}/d_{xz} \rightarrow \text{LUMO}$	491 (413)	490 (437)	508 (478)	530 (475)
III	$\pi\text{-ligand} + d_z \rightarrow \text{LUMO}$	533 (443) <sup>a</sup>	430 (410)	464 (448)	488 (449)

<sup>a</sup> Pure Ni  $d_z \rightarrow \text{LUMO}$  transition.

For  $\text{NiLH}_3$ , the d-orbital manifold is consistent with that expected for a trigonal-planar metal center with three  $\sigma$ -donors: the degenerate  $d_{xy}/d_{x^2-y^2}$  orbitals are the most destabilized, followed by  $d_z$ , and then the  $d_{xz}/d_{yz}$  set. For **1–3**, the presence of the supporting group 13 metal ion results in the stabilization of the Ni  $3d_z$  orbital *via* Ni  $\rightarrow \text{M}(\text{p}_z/\text{s})$  dative bonding, which is consistent with the blue shift in the predicted pure  $3d_z \rightarrow \text{LUMO}$  transitions in the bimetallic NiML complexes (363 to 385 nm; Table S30†) relative to  $\text{NiLH}_3$  (443 nm). The Ni  $d_{xz}/d_{yz}$  orbitals, on the other hand, are destabilized upon the introduction of the supporting metal and its variation down group 13. Presumably, the  $\pi$ -back-bonding interaction, Ni  $d_{xz}/d_{yz} \rightarrow \text{P-C } \sigma^*$ , becomes weaker as the Ni center becomes more electron-deficient due to stronger electron withdrawal by the supporting metal (In > Ga > Al > no support).<sup>16</sup> In support, both the Ni–P bonds elongate and the <sup>31</sup>P NMR signal shifts downfield from  $\text{NiLH}_3$  to **1** to **2** to **3**.

Another notable MO trend involves the energy difference between the Ni  $d_{xz}/d_{yz}$  orbitals and the LUMO, as reflected in the peak II energies, which decrease upon the introduction and variation of the supporting metal down group 13. This particular energy gap is important because the LUMO and the Ni  $d_{xz}/d_{yz}$  orbitals are the frontier Ni-based MOs that participate in small-molecule binding, with the Ni-based LUMO accepting  $\sigma$ -donation from either the H<sub>2</sub>  $\sigma$ -bond or the N<sub>2</sub> lone pair, and the Ni  $d_{xz}/d_{yz}$  orbitals participating in  $\pi$ -back-bonding to either the H<sub>2</sub>  $\sigma^*$  or N<sub>2</sub>  $\pi^*$  LUMOs. Overall, the Ni  $d_{xz}/d_{yz} \rightarrow \text{LUMO}$  excitation energy decreases by  $\sim 0.2$  eV across the NiML complexes, from 2.53 eV in **1** to 2.44 eV in **2** to 2.34 eV in **3** (Table S28†). Thus, it is reasonable to propose that varying the supporting metal from Al to Ga to In results in the destabilization of the Ni  $d_{xz}/d_{yz}$  orbital set and the stabilization of the Ni-based LUMO, such that both become more energetically accessible to interact with small-molecule substrates.

The involvement of the LUMO in small-molecule binding is further supported by examining the changes in the UV-Vis spectra for **3** upon binding H<sub>2</sub> and N<sub>2</sub> (Fig. 5c). Notably, both the experimental and theoretical spectra of **3-H<sub>2</sub>** and **3-N<sub>2</sub>** lack any intense features between 400 and 700 nm. Instead, the lowest energy transitions for **3-H<sub>2</sub>** and **3-N<sub>2</sub>** are predicted at 375 and 391 nm, respectively. The shift to higher energy excitations for the H<sub>2</sub> and N<sub>2</sub> adducts can be qualitatively explained by the nature of their acceptor MOs, which we define as the lowest-energy unoccupied MO with significant Ni character, rather





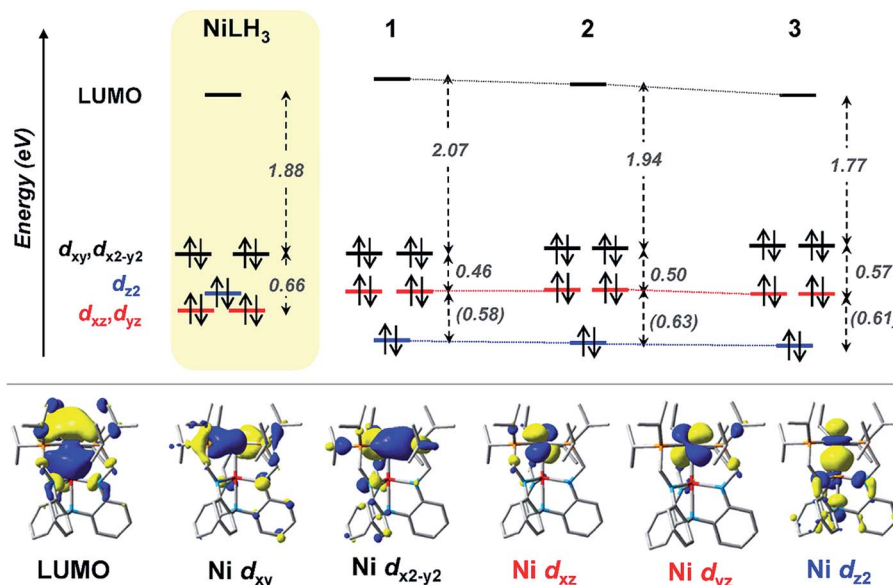


Fig. 6 (Top) MO diagrams of  $\text{NiLH}_3$  and complexes 1–3. The ligand field energies (in eV) are based on UV-Vis data (Table 5). TD-DFT calculated energies are shown (in eV, italicized within parentheses) when experimental values were not obtainable. (Bottom) MOs for complex 2, which are representative of those for the series. Note that MO energies are drawn to scale, but energy comparisons across the complexes are qualitative.

than those that are ligand based (Fig. S60–S63 and Tables S33–S38†). For both 3- $\text{H}_2$  and 3- $\text{N}_2$ , the acceptor MO appears to be an anti-bonding combination of the LUMO in 3 and the donor MO of the small molecule (Fig. S64†). Thus, upon small-molecule binding *via* the dominant  $\sigma$ -donation interaction with the LUMO of  $\text{NiML}$ , the resulting acceptor orbitals in  $(\text{L}')\text{NiML}$  adducts ( $\text{L}' = \text{H}_2, \text{N}_2$ ) to which electrons can be excited are of higher energy relative to the Ni 3d manifold, and thereby give rise to higher energy electronic transitions.

## Part V. Linear free-energy relationships

We examined linear free-energy relationships across the  $\text{NiML}$  series to quantify the effect of the supporting group 13 metal on the thermodynamics and kinetics of small-molecule binding. For  $\text{H}_2$  binding, an excellent correlation was observed between the thermodynamic free energies ( $\Delta G^\circ_{1\text{M}}$ ) and the free energies

of activation ( $\Delta G^\ddagger_{\text{bind}}$ ), where more exergonic binding equilibria have smaller activation barriers ( $R^2 = 0.999$ , Fig. 7a). The slope of +0.93 in the  $\Delta G^\ddagger_{\text{bind}}$  versus  $\Delta G^\circ_{1\text{M}}$  plot indicates that a decrease of  $\sim 1 \text{ kcal mol}^{-1}$  in  $\Delta G^\circ_{1\text{M}}$  for  $\text{H}_2$  binding corresponds to a commensurate lowering of the free energy barrier. Reasonably strong correlations were also found between the Ni 3d<sub>xz</sub>/d<sub>yz</sub> → LUMO excitation energy and  $\Delta G^\circ$  for  $\text{H}_2$  ( $R^2 = 0.924$ ) and  $\text{N}_2$  ( $R^2 = 0.963$ ) binding (Fig. 7b). This correlation makes sense since the Ni 3d<sub>xz</sub>/d<sub>yz</sub> orbitals and the LUMO are the Ni-based frontier orbitals that participate in small-molecule binding (*vide supra*). The slopes of the plots of  $\Delta G^\circ$  for  $\text{H}_2$  and  $\text{N}_2$  binding *versus* the Ni 3d<sub>xz</sub>/d<sub>yz</sub> → LUMO excitation energy (in  $\text{kcal mol}^{-1}$ ) are close to unity, where a decrease of 1  $\text{kcal mol}^{-1}$  in the Ni 3d<sub>xz</sub>/d<sub>yz</sub> → LUMO excitation energy is associated with a nearly equivalent increase in the favorability of  $\text{H}_2/\text{N}_2$  binding.

The isostructural nature of the  $(\eta^2\text{-H}_2)\text{NiML}$  series allows us to further interrogate which intrinsic properties of the group 13

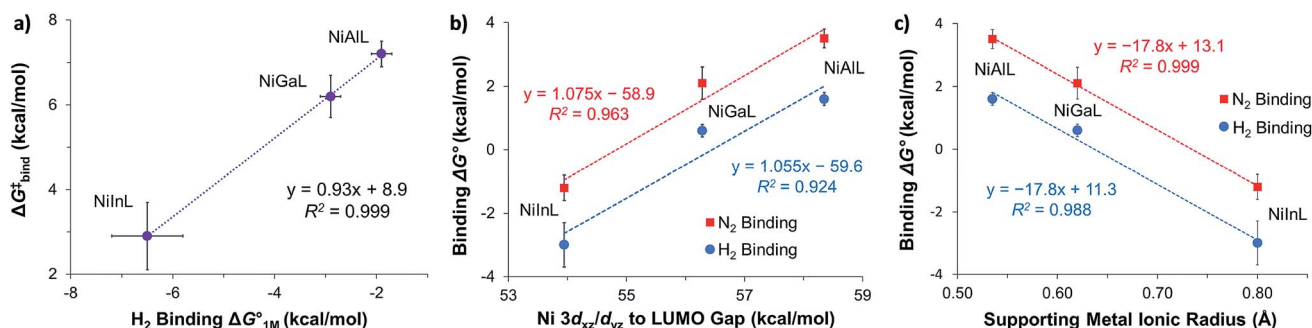


Fig. 7 (a) Plot of free energy barrier for  $\text{H}_2$  binding ( $\Delta G^\ddagger_{\text{bind}}$ ) vs. thermodynamic free energy for  $\text{H}_2$  binding ( $\Delta G^\circ_{1\text{M}}$ ), with the standard deviation in all values shown by error bars and all standard states defined to be  $[\text{H}_2] = 1 \text{ M}$  in toluene- $d_8$ . (b–c) Plots of  $\Delta G^\circ$  for  $\text{H}_2$  (blue circles) and  $\text{N}_2$  binding (red squares) vs. Ni 3d<sub>xz</sub>/d<sub>yz</sub> to LUMO energy gap (b) and vs. supporting metal Shannon ionic radii (c). Ni 3d<sub>xz</sub>/d<sub>yz</sub> to LUMO energy gaps were measured experimentally by UV-Vis spectroscopy with transition assignments from TD-DFT calculations (see ESI† and Table 5).



support (M) dictate the favorability of H<sub>2</sub> and N<sub>2</sub> binding. A strong negative correlation was found between the size of the supporting metal, as represented by Shannon's M(III) ionic radii,<sup>60</sup> and  $\Delta G^\circ$  for both H<sub>2</sub> ( $R^2 = 0.988$ ) and N<sub>2</sub> ( $R^2 = 0.999$ ) binding (Fig. 7c), where larger supporting ions induce more exergonic binding. The finding that larger supporting metals better poise Ni for small-molecule binding is likely a composite effect of both electronic and steric factors. Larger group 13 supporting metals show stronger Ni→M bonding interactions (Table S24b†) and shift the Ni(0/I) oxidation to more positive potentials,<sup>16</sup> both of which should lower the Pauli repulsion associated with binding a donor (Fig. S71†). Also, larger group 13 ions force Ni to move further above the P<sub>3</sub>-plane which should minimize the structural reorganization energy associated with small-molecule binding (Fig. S72†).

The confluence of steric and electronic effects is also supported by the fact that neither effect can solely account for the observed trends. For example, the position of Ni above the P<sub>3</sub>-plane is identical for both Al and Ga (0.13 Å), despite their distinct differences in  $\Delta G^\circ$  for H<sub>2</sub>/N<sub>2</sub> binding. Also, correlations between  $\Delta G^\circ$  for H<sub>2</sub>/N<sub>2</sub> binding and Ni redox potentials are comparatively poor, whether one considers the Ni(0/I) oxidation or the Ni(−I/0) reduction potentials ( $R^2 = 0.726$  to  $0.891$ , Fig. S68 and S69†).<sup>16,61</sup> Typically Lewis acidity is expected to correlate with  $\sigma$ -accepting ability, yet no linear relationship exists between  $\Delta G^\circ$  for H<sub>2</sub>/N<sub>2</sub> binding and the relative Lewis acidities of group 13 metals, as given by the pK<sub>a</sub> values of the corresponding M(H<sub>2</sub>O)<sub>6</sub><sup>3+</sup> complexes ( $R^2 = 0.02$ – $0.05$ , Fig. S66†).<sup>62,63</sup> It is plausible that the Lewis acidity scale based on M–OH<sub>2</sub> bonds, where H<sub>2</sub>O is the Lewis base, is an inappropriate benchmark for a Ni(0) Lewis base. You and Gabbaï have recently proposed that the double-decker ligand framework, which imposes spatial constraints, may “accentuate” the influence of the group 13 ion's size.<sup>64</sup> It is noteworthy that  $\Delta G^\circ$  values for H<sub>2</sub> ( $R^2 = 0.945$ ) and N<sub>2</sub> ( $R^2 = 0.977$ ) binding correlate reasonably well with the degree of Ni→M dative bonding, as quantified by the ratio of the solid-state Ni–M bond distance to the sum of the covalent radii of Ni and M (Fig. S67†).<sup>65,66</sup> This finding is consistent with the hypothesis that group 13 metals can significantly tune the reactivity of a proximal Ni center *via* a direct Ni(0)→M(III) dative interaction.

## Conclusion

H<sub>2</sub> and N<sub>2</sub> binding is atypical for Ni complexes and facilitating H<sub>2</sub> activation to form reactive Ni( $\eta^2$ -H<sub>2</sub>) and/or Ni–H species poses a difficult hurdle for developing homogeneous Ni catalysts for H<sub>2</sub> oxidation, proton reduction, and related processes. Excitingly, we find that supporting Ni with group 13 metals induces the binding of H<sub>2</sub> and N<sub>2</sub> to Ni, with H<sub>2</sub> binding found to be  $\sim 2$  kcal mol<sup>−1</sup> more favorable than N<sub>2</sub> binding in each case. The pivotal role of the supporting metal in promoting binding to the NiML complexes is highlighted by the inability of NiLH<sub>3</sub>, a similarly ligated mononuclear Ni center, to bind H<sub>2</sub> or N<sub>2</sub> under any conditions examined. The dramatic tuning effect of the supporting group 13 metal is illustrated by the wide range of  $\Delta G^\circ$  values for H<sub>2</sub> binding, which span  $\sim 8$  kcal mol<sup>−1</sup>

(including NiLH<sub>3</sub>) and nearly cover the entire range of previously reported values. H<sub>2</sub> binding to NiInL (3) is more exergonic than any such equilibrium reported, allowing for solid-state characterization of ( $\eta^2$ -H<sub>2</sub>)NiInL (3-H<sub>2</sub>) *via* neutron diffraction, which is unprecedented for an H<sub>2</sub> adduct of Ni or any d<sup>10</sup> metal.

Theoretical calculations have provided important insights into the role of the supporting metal in promoting small-molecule binding. Specifically, complementary  $\sigma$ -interactions are proposed based on ETS-NOCV calculations, where H<sub>2</sub> → Ni  $\sigma$ -donation to the energetically-accessible Ni(4p<sub>z</sub>)-based LUMO is the dominant binding interaction, which is likely induced by electron withdrawal from Ni *via* the dative Ni(0)→M(III) bond. The involvement of the LUMO in small-molecule binding is supported by TD-DFT and UV-Vis studies, along with the strong correlation between  $\Delta G^\circ$  values for H<sub>2</sub>/N<sub>2</sub> binding and the Ni 3d<sub>xz</sub>/d<sub>yz</sub> → LUMO excitation energy. Notably, the size of the supporting M(III) ion correlates best with  $\Delta G^\circ$  values for H<sub>2</sub> and N<sub>2</sub> binding, with larger group 13 supporting metals inducing more favorable binding by: rendering Ni more electron-deficient, favoring stronger Ni→M interaction, and minimizing the structural reorganization energy. Moreover, thermodynamically favorable H<sub>2</sub> binding equilibria (In > Ga > Al) have proportionally smaller free energies of activation.

Overall, a thorough understanding of H<sub>2</sub> and N<sub>2</sub> binding to NiML complexes, and the integral role of the supporting metal therein, has been presented. Future work will explore the impact of the thermodynamics and kinetics of H<sub>2</sub> binding equilibria on catalytic CO<sub>2</sub> hydrogenation reactivity, where H<sub>2</sub> binding to displace formate has been found to be the rate-determining step in catalysis.<sup>20,67</sup> Additionally, the generalizability of the strategy of favorably altering base-metal reactivity *via* interactions with group 13 supporting metals will be assessed, and efforts are currently underway to extend our studies to other ligand frameworks and transition metals.

## Experimental section

Additional information is provided in the ESI.†

### General considerations

Unless otherwise stated, all manipulations were performed under an Ar or N<sub>2</sub> atmosphere inside a glovebox or using standard Schlenk techniques. Standard solvents were deoxygenated by sparging with N<sub>2</sub> and dried by passing through activated alumina columns of a SG water solvent purification system. Deuterated solvents and HD gas (97% D content) were purchased from Cambridge Isotope Laboratories, Inc. Deuterated solvents were degassed *via* freeze–pump–thaw cycles, and either stored over activated 4 Å molecular sieves or stirred with Na–K alloy and distilled. N<sub>2</sub> and H<sub>2</sub> gases were purchased from Matheson Trigas, Inc., and a gas mixture of 10% H<sub>2</sub>/90% Ar was purchased from Praxair, Inc. All other reagents were purchased from commercial vendors and used without purification unless otherwise noted. The ligand N(*o*-(NHCH<sub>2</sub>P<sup>i</sup>Pr<sub>2</sub>)C<sub>6</sub>H<sub>4</sub>)<sub>3</sub> (abbreviated as LH<sub>3</sub>), NiAlL (1), NiGaL (2), NiInL (3), ( $\eta^2$ -H<sub>2</sub>)NiGaL (2-H<sub>2</sub>), (N<sub>2</sub>)NiInL (3-N<sub>2</sub>), ( $\eta^2$ -H<sub>2</sub>)NiInL (3-H<sub>2</sub>), and NiLH<sub>3</sub> (4) were



synthesized according to the literature.<sup>16,34,68</sup>  $^1\text{H}$  and  $^{31}\text{P}$  NMR spectra were recorded on Bruker (400 or 500 MHz) or Varian (500 MHz) spectrometers and referenced to internal residual solvent (or  $\text{H}_3\text{PO}_4$  for  $^{31}\text{P}$  NMR spectra). For VT NMR experiments, the temperature was calibrated using a methanol ( $\leq 298$  K) or an ethylene glycol ( $> 298$  K) standard. UV-Vis spectra were collected on a Cary-14 instrument. Cyclic voltammetry experiments were performed using a CHI Instruments 620D potentiostat. The one-cell setup utilized a glassy carbon working electrode, platinum wire counter electrode, and  $\text{Ag}/\text{AgNO}_3$  reference electrode in  $\text{CH}_3\text{CN}$ .

### *In situ* generation of $(\eta^2\text{-H}_2)\text{NiAlL}$ (abbreviated as 1-H<sub>2</sub>)

A solution of **1** (15 mg, 19.6  $\mu\text{mol}$ ) in  $\text{THF-d}_8$  ( $\sim 0.30$  mL) was added to a PEEK NMR cell and pressurized to 34 atm  $\text{H}_2$ . The following NMR data are reported at 34 atm  $\text{H}_2$ ; an equilibrium between **1** and 1-H<sub>2</sub> can also be observed under 1 atm  $\text{H}_2$  at low  $T$ .  $^1\text{H}\{^{31}\text{P}\}$  NMR (ppm,  $\text{THF-d}_8$ , 232 K, 500 MHz): 7.34 (br, 3H, ArH), 6.87 (br, 3H, ArH), 6.34 (br, 6H, ArH), 3.00 (br, 3H,  $\text{CHH}'$ ), 2.87 (br, 3H,  $\text{CHH}'$ ), 2.10 (m, 6H,  $\text{CH}(\text{CH}_3)_2$ ), 1.27 to 0.90 (36H,  $\text{CH}(\text{CH}_3)_2$ ),  $-1.5$  (br, 2H,  $(\text{H}_2)\text{Ni}$ ,  $T_1$  (min)  $\leq 0.49(5)$  s at 200 K).  $^{31}\text{P}$  NMR (ppm, 200 K, 202.4 MHz): 44.9 (in  $\text{THF-d}_8$ ), or  $\sim 44.3$  (in toluene- $\text{d}_8$ ). The lability of  $\text{H}_2$  precluded elemental analysis from being obtained.

### *In situ* observation of $(\text{N}_2)\text{NiAlL}$ (1-N<sub>2</sub>) and $(\text{N}_2)\text{NiGaL}$ (2-N<sub>2</sub>)

A solution of **1** (3.7 mg, 4.8  $\mu\text{mol}$ ) in toluene- $\text{d}_8$  (0.30 mL) was added to a PEEK NMR cell and pressurized to 51 atm  $\text{N}_2$ . Similarly, a solution of **2** (5.0 mg, 6.2  $\mu\text{mol}$ ) in toluene- $\text{d}_8$  (0.41 mL) was added to a J. Young NMR tube under 1 atm  $\text{N}_2$ . Neither 1-N<sub>2</sub> nor 2-N<sub>2</sub> was isolable due to lability of the  $\text{N}_2$  ligand. Both 1-N<sub>2</sub> and 2-N<sub>2</sub> were observed in the presence of **1** and **2**, respectively, which limited  $^1\text{H}$  NMR characterization due to overlapping resonances. For 1-N<sub>2</sub>:  $^{31}\text{P}$  NMR (ppm, toluene- $\text{d}_8$ , 190 K, 51 atm  $\text{N}_2$ , 202.4 MHz):  $\sim 32.2$ . For 2-N<sub>2</sub>:  $^{31}\text{P}$  NMR (ppm, toluene- $\text{d}_8$ , 193 K, 1 atm  $\text{N}_2$ , 162 MHz):  $\sim 43.5$ .

### X-ray and neutron diffraction crystallographic and structure refinement details

**X-ray diffraction.** A gold block of  $(\eta^2\text{-H}_2)\text{NiInL}$  (3-H<sub>2</sub>) was placed onto the tip of a MiTeGen Dual-Thickness Micro-Loop™ and mounted on a Bruker Photon II CMOS diffractometer for data collection at 100(2) K (Table 6). The data collections were carried out using Mo  $K\alpha$  radiation (graphite monochromator), and the data intensity was corrected for absorption and decay (SADABS).<sup>69</sup> Final cell constants were obtained from least-squares fits of all measured reflections. The structure was solved using SHELXT-16 and refined using SHELXL-16, which were executed from the ShelXle graphical user interface.<sup>70</sup> A direct-methods solution was calculated which provided most non-hydrogen atoms from the E-map. Full-matrix least-squares/difference Fourier cycles were performed to locate the remaining non-hydrogen atoms. All non-hydrogen atoms were refined with anisotropic displacement parameters. Hydrogen atoms were placed in ideal positions and refined as riding atoms with relative isotropic

Table 6 Crystallographic details for 3-H<sub>2</sub> (X-ray and neutron structures)

Radiation type	X-ray	Neutron
Chemical formula	$\text{C}_{39}\text{H}_{62}\text{N}_4\text{P}_3\text{InNi}$	$\text{C}_{39}\text{H}_{62}\text{N}_4\text{P}_3\text{InNi}$
$F_w$	853.36	853.36
Cryst syst	Orthorhombic	Orthorhombic
Space group	$P2_12_12_1$	$P2_12_12_1$
$a$ (Å)	12.2127(4)	12.2010(10)
$b$ (Å)	14.5402(5)	14.5638(12)
$c$ (Å)	22.5601(8)	22.547(2)
$\alpha$ (deg)	90	90
$\beta$ (deg)	90	90
$\gamma$ (deg)	90	90
$V$ (Å <sup>3</sup> )	4006.1(2)	4006.4(6)
$Z$	4	4
$\lambda$ (Å), $\mu$ (mm <sup>-1</sup> )	0.71073, 1.198	0.60–3.36, 0.1570 + 0.1306 $\lambda$
$T$ (K)	100(2)	100(2)
$\Theta$	2.285 to 36.348	7.352 to 78.740
Reflns collected	237 431	14 303
Unique reflns	19 473	4718
Data/restraint/parameters	19 473/0/451	4718/1068/991
$R1$ , $wR2$ ( $I > 2\sigma(I)$ )	0.0181, 0.0392	0.0620, 0.1262

displacement parameters,<sup>71</sup> with the exception of the apical  $\text{H}_2$  ligand in 3-H<sub>2</sub>, for which the H atoms were sufficiently resolved in the Fourier difference map to allow tentative placement. Images were rendered using POV-ray.<sup>72</sup>

**Neutron diffraction.** Neutron diffraction data were collected using the TOPAZ single-crystal time-of-flight (TOF) Laue diffractometer at the Spallation Neutron Source (SNS), at Oak Ridge National Laboratory (Oak Ridge, TN).<sup>73</sup> A block-shaped crystal of 3-H<sub>2</sub>, with dimensions of  $0.35 \times 0.30 \times 0.30$  mm, was grown from a concentrated toluene solution under 1 atm  $\text{H}_2$  at  $\sim 280$  K for several weeks. The crystal was mounted on the tip of a polyimide capillary using fluorinated grease and transferred to the TOPAZ goniometer for data collection at 100 K (Table 6). To ensure good coverage and redundancy, data were collected using crystal orientations optimized with CrystalPlan software<sup>74</sup> for optimal coverage of symmetry-equivalent reflections of the orthorhombic cell. The integrated raw Bragg intensities were obtained using the 3-D ellipsoidal Q-space integration in accordance with previously reported methods.<sup>75</sup> Data reduction, including neutron TOF spectrum, Lorentz, and detector efficiency corrections, was carried out with the ANVRED3 program.<sup>76</sup> A spherical absorption correction was applied with  $\mu = 0.1570 + 0.1306 \lambda \text{ cm}^{-1}$ . The reduced data were saved as SHELX HKLF2 format, in which the wavelength is recorded separately for each reflection, and data were not merged. Starting with the X-ray structure at 100 K as an input model (where all the H atoms were placed except for the  $\text{H}_2$  ligand), the neutron crystal structure was refined using the SHELXL-14/7 program<sup>70,71</sup> with RIGU restraints for the H-atoms' anisotropic displacement parameters.<sup>77</sup>

### General procedure for $\text{H}_2/\text{N}_2$ binding studies

A toluene- $\text{d}_8$  solution of NiML (15 mM) was filtered and transferred to either a J. Young NMR tube ( $\leq 3.8$  atm) or a PEEK NMR





cell ( $\geq 6.8$  atm).<sup>78,79</sup> For high-pressure studies, the PEEK cell was sealed and connected to a high-pressure line equipped with a vacuum pump and an ISCO syringe pump. The line was purged with H<sub>2</sub> or N<sub>2</sub> gas three times. Next, the headspace was degassed by opening the PEEK cell to static vacuum ( $3 \times 30$  s), and H<sub>2</sub> or N<sub>2</sub> gas was then delivered to the cell from an ISCO syringe pump running constantly at the desired pressure (*i.e.* continuous gas feed). The contents of the PEEK cell were mixed using a vortex mixer for  $\sim 15$  min prior to NMR data collection to allow for pressure stabilization and equilibration. For low-pressure studies, J. Young NMR tubes were pressurized after freeze–pump–thaw cycles. VT <sup>31</sup>P NMR spectra were acquired at several different *T* (193 to 368 K) in all studies, with an adequate number of scans collected (typically 64 to 160 scans) to quantify the observed peak position (for fast chemical exchange) and/or the relative peak integrations (for slow chemical exchange). <sup>31</sup>P spectra were typically collected with a recycle delay time of 2 s and an acquisition time of 1.68 s. In cases where quantitative integration of multiple peaks was desired, a longer delay time of 10 s was used.

**CAUTION:** H<sub>2</sub> is a highly flammable gas. Pressurized vessels must be handled with care using proper personal protective equipment. PEEK cells were employed for the high-pressure NMR studies, as described previously.<sup>78,79</sup>

### General procedure for kinetic studies of H<sub>2</sub> self-exchange

A solution of NiML (7.5 mM in 0.70 mL) was prepared in toluene-*d*<sub>8</sub> and transferred to a J. Young NMR tube. VT <sup>31</sup>P NMR spectra were obtained at various *T* ( $\geq 7$  data points, 214 K to 344 K) for samples under 1 atm Ar to determine intrinsic linewidths and chemical shifts for NiML complexes. Subsequently, after freeze–pump–thaw cycles, the VT <sup>31</sup>P NMR profile was obtained under 1 atm H<sub>2</sub>. NMR lineshape analysis was performed using the gNMR (version 5.0) program<sup>80</sup> to extract H<sub>2</sub> self-exchange rates at each *T* (see ESI† for details†). <sup>31</sup>P NMR spectra were typically collected with a delay time of 2 s, an acquisition time of 1.68 s, and with 160 scans.

### Computational methods

**Density functional theory (DFT).** DFT calculations were performed using the Gaussian 09 program package.<sup>81</sup> Four functionals (M06-L,<sup>38</sup> M06-D3,<sup>56,57</sup> PBE0,<sup>82</sup> and PBE0-D3<sup>56,82</sup>) and five basis sets (denoted as bs0 to bs4, Table S3†) were evaluated. The M06-L/bs1 method (def2-TZVPP for H<sub>2</sub>, N<sub>2</sub>, Ni, Al, Ga, and In, with the SDD effective core potential<sup>83</sup> for In; def2-TZVP basis set for N, P; and def2-SVP for C and H atoms)<sup>84</sup> gave the best match to the experimental binding energies, and had been used in related prior studies.<sup>67</sup> Geometric structures were optimized in the gas phase at 0 K, using the crystal structure atomic coordinates as the initial geometries when available (1–3, 3-H<sub>2</sub>, and 3-N<sub>2</sub>). Vibrational frequency analyses were performed with the harmonic approximation to confirm the nature of all species (0 and 1 imaginary frequency for ground-state and transition-state structures, respectively). Unless otherwise noted, Gibbs free energies at 298.15 K and 1 atm were computed by adding zero-point vibrational energies and thermal corrections. Solvation effects

were considered by performing single-point calculations for all stationary points using the SMD solvation model.<sup>85</sup> The H<sub>2</sub> and N<sub>2</sub> binding energies for NiML were calculated according to the following equation:



In eqn (3), *X*<sub>(g)</sub> is H<sub>2</sub> or N<sub>2</sub>, and the standard state is defined as 1 atm for *X*<sub>(g)</sub>. The overall energy for eqn (3) was determined based on the gas-phase free energies for H<sub>2</sub> or N<sub>2</sub> and the Gibbs free energies with solvation (in toluene) for NiML<sub>(solv)</sub> and *X*-NiML<sub>(solv)</sub>.

**Energy decomposition analysis (EDA).** The EDA method<sup>58</sup> was implemented in the Amsterdam Density Functional (ADF 2016)<sup>86,87</sup> program package to study chemical bonding between H<sub>2</sub> and Ni in the (η<sup>2</sup>-H<sub>2</sub>)NiML complexes. Single-point energy calculations were performed using PBE0-D3/TZ2P<sup>88</sup> on the M06-L/bs1-optimized geometries. Relativistic effects for In were included by applying the zeroth-order regular approximation (ZORA).<sup>89</sup>

EDA breaks the total interaction energy ( $\Delta E_{\text{int}}$ ) between the H<sub>2</sub> and NiML fragments into four components, as shown in eqn (4):

$$\Delta E_{\text{int}} (\text{EDA}) = \Delta E_{\text{elstat}} + \Delta E_{\text{Pauli}} + \Delta E_{\text{orb}} + \Delta E_{\text{disp}} \quad (4)$$

$\Delta E_{\text{elstat}}$  is the attractive, quasi-classical electrostatic interaction between the electrons and the nuclei;  $\Delta E_{\text{Pauli}}$  is the repulsive interaction between the occupied orbitals of the fragments;  $\Delta E_{\text{orb}}$  is the interaction between the occupied molecular orbitals of one fragment and the unoccupied molecular orbitals of the other fragment; and,  $\Delta E_{\text{disp}}$  corresponds to the dispersive effects between the two fragments. The extended transition state—natural orbitals for chemical valence (ETS-NOCV) method,<sup>59</sup> in combination with the energy decomposition scheme, was utilized to break down the orbital interaction component ( $\Delta E_{\text{orb}}$ ) into contributions from specific NOCV pairs (see ESI† for further details†).

**Time-dependent (TD) DFT calculations.** TD-DFT calculations (M06-D3/bs4, Gaussian 09) with solvent considerations (SMD, THF) were performed to aid in assigning electronic transitions in the absorption spectra of NiLH<sub>3</sub> (4), NiML (1–3), (η<sup>2</sup>-H<sub>2</sub>)NiML, and (N<sub>2</sub>)NiML complexes (M = Al, Ga, In). The basis sets denoted by bs4 were used: LANL2DZ<sup>90</sup> for In and 6-311G(d,p)<sup>91</sup> for all other atoms.

## Conflicts of interest

The authors declare no competing financial interests.

## Acknowledgements

The authors thank Prof. Laura Gagliardi, Prof. Chris Cramer, Dr Molly O'Hagan, Dr Adrian Houghton, and Dr Tom Autrey for helpful discussions. James Moore is acknowledged for assistance with X-ray diffraction. R. C. C. was supported by the DOE Office of Science Graduate Student Research and the UMN Doctoral Dissertation Fellowship programs. M. V. V. was



supported by the NSF Graduate Research Fellowship. C. C. L. acknowledges NSF (CHE-1665010) for support of the experimental work. J. X., J. Y., and K. D. V. were supported as part of the Inorganometallic Catalyst Design Center, an Energy Frontier Research Center funded by the U.S. Department of Energy (DOE), Office of Science, Basic Energy Sciences under Award DE-SC0012702. S. A. B., J. C. L., and A. M. A. were supported by the U.S. Department of Energy, Office of Science, Office of Basic Energy Sciences, Division of Chemical Sciences, Geosciences & Biosciences. Single crystal neutron diffraction experiment performed on TOPAZ used resources at the Spallation Neutron Source, a DOE Office of Science User Facility operated by the Oak Ridge National Laboratory, under Contract No. DE-AC05-00OR22725 with UT-Battelle, LLC. X-ray diffraction experiments were performed using a crystal diffractometer acquired through an NSF-MRI award (CHE-1229400).

## References

- 1 L. Alig, M. Fritz and S. Schneider, *Chem. Rev.*, 2019, **119**, 2681–2751.
- 2 S. J. C. Robinson and D. M. Heinekey, *Chem. Commun.*, 2017, **53**, 669–676.
- 3 R. H. Morris, *Acc. Chem. Res.*, 2015, **48**, 1494–1502.
- 4 P. J. Chirik, *Acc. Chem. Res.*, 2015, **48**, 1687–1695.
- 5 R. M. Bullock and M. L. Helm, *Acc. Chem. Res.*, 2015, **48**, 2017–2026.
- 6 R. H. Crabtree, *Chem. Rev.*, 2016, **116**, 8750–8769.
- 7 G. J. Kubas, *Chem. Rev.*, 2007, **107**, 4152–4205.
- 8 P. G. Jessop and R. H. Morris, *Coord. Chem. Rev.*, 1992, **121**, 155–284.
- 9 G. J. Kubas, *Catal. Lett.*, 2005, **104**, 79–101.
- 10 J. M. Millar, R. V. Kastrup, M. T. Melchior, I. T. Horvath, C. D. Hoff and R. H. Crabtree, *J. Am. Chem. Soc.*, 1990, **112**, 9643–9645.
- 11 A. A. Gonzalez and C. D. Hoff, *Inorg. Chem.*, 1989, **28**, 4295–4297.
- 12 D. G. Abrecht and B. Fultz, *J. Phys. Chem. C*, 2012, **116**, 22245–22252.
- 13 D. E. Prokopchuk, G. M. Chambers, E. D. Walter, M. T. Mock and R. M. Bullock, *J. Am. Chem. Soc.*, 2019, **141**, 1871–1876.
- 14 D. L. M. Suess, C. Tsay and J. C. Peters, *J. Am. Chem. Soc.*, 2012, **134**, 14158–14164.
- 15 M. V. Vollmer, J. Xie and C. C. Lu, *J. Am. Chem. Soc.*, 2017, **139**, 6570–6573.
- 16 R. C. Cammarota and C. C. Lu, *J. Am. Chem. Soc.*, 2015, **137**, 12486–12489.
- 17 B. R. Barnett, C. E. Moore, P. Chandrasekaran, S. Sproules, A. L. Rheingold, S. DeBeer and J. S. Figueroa, *Chem. Sci.*, 2015, **6**, 7169–7178.
- 18 T.-P. Lin, C. R. Wade, L. M. Pérez and F. P. Gabbaï, *Angew. Chem., Int. Ed.*, 2010, **49**, 6357–6360.
- 19 T.-P. Lin, R. C. Nelson, T. Wu, J. T. Miller and F. P. Gabbaï, *Chem. Sci.*, 2012, **3**, 1128–1136.
- 20 R. C. Cammarota, M. V. Vollmer, J. Xie, J. Ye, J. C. Linehan, S. A. Burgess, A. M. Appel, L. Gagliardi and C. C. Lu, *J. Am. Chem. Soc.*, 2017, **139**, 14244–14250.
- 21 J. Takaya and N. Iwasawa, *J. Am. Chem. Soc.*, 2017, **139**, 6074–6077.
- 22 P. Steinhoff, M. Paul, J. P. Schroers and M. E. Tauchert, *Dalton Trans.*, 2019, **48**, 1017–1022.
- 23 B. A. Connor, J. Rittle, D. VanderVelde and J. C. Peters, *Organometallics*, 2016, **35**, 686–690.
- 24 W. H. Harman, T. P. Lin and J. C. Peters, *Angew. Chem., Int. Ed.*, 2014, **53**, 1081–1086.
- 25 R. H. Morris and R. J. Wittebort, *Magn. Reson. Chem.*, 1997, **35**, 243–250.
- 26 P. A. Maltby, M. Schlaf, M. Steinbeck, A. J. Lough, R. H. Morris, W. T. Klooster, T. F. Koetzle and R. C. Srivastava, *J. Am. Chem. Soc.*, 1996, **118**, 5396–5407.
- 27 G. J. Kubas, C. J. Burns, J. Eckert, S. W. Johnson, A. C. Larson, P. J. Vergamini, C. J. Unkefer, G. R. K. Khalsa, S. A. Jackson and O. Eisenstein, *J. Am. Chem. Soc.*, 1993, **115**, 569–581.
- 28 N. A. Eberhardt and H. Guan, *Chem. Rev.*, 2016, **116**, 8373–8426.
- 29 W. A. Gunderson, D. L. M. Suess, H. Fong, X. Wang, C. M. Hoffmann, G. E. Cutsail, J. C. Peters and B. M. Hoffman, *J. Am. Chem. Soc.*, 2014, **136**, 14998–15009.
- 30 R. S. Rowland and R. Taylor, *J. Phys. Chem.*, 1996, **100**, 7384–7391.
- 31 J. Halpern, L. Cai, P. J. Desrosiers and Z. Lin, *J. Chem. Soc., Dalton Trans.*, 1991, 717–723.
- 32 R. H. Crabtree and D. G. Hamilton, *J. Am. Chem. Soc.*, 1986, **108**, 3124–3125.
- 33 T. A. Luther and D. M. Heinekey, *Inorg. Chem.*, 1998, **37**, 127–132.
- 34 L. J. Clouston, R. B. Siedschlag, P. A. Rudd, N. Planas, S. Hu, A. D. Miller, L. Gagliardi and C. C. Lu, *J. Am. Chem. Soc.*, 2013, **135**, 13142–13148.
- 35 M. P. Williamson, *Prog. Nucl. Magn. Reson. Spectrosc.*, 2013, **73**, 1–16.
- 36 R. G. Bryant, *J. Chem. Educ.*, 1983, **60**, 933–935.
- 37 J. Feeney, J. G. Batchelor, J. P. Albrand and G. C. K. Roberts, *J. Magn. Reson.*, 1979, **33**, 519–529.
- 38 Y. Zhao and D. G. Truhlar, *J. Chem. Phys.*, 2006, **125**, 194101.
- 39 D. M. Heinekey, M. H. Voges and D. M. Barnhart, *J. Am. Chem. Soc.*, 1996, **118**, 10792–10802.
- 40 B. E. Hauger, D. Gusev and K. G. Caulton, *J. Am. Chem. Soc.*, 1994, **116**, 208–214.
- 41 D. G. Gusev, A. B. Vymenits and V. I. Bakhmutov, *Inorg. Chem.*, 1992, **31**, 1–2.
- 42 M. Mediati, G. N. Tachibana and C. M. Jensen, *Inorg. Chem.*, 1990, **29**, 3–5.
- 43 D. G. Gusev, V. I. Bakhmutov, V. V. Grushin and M. E. Vol'pin, *Inorg. Chim. Acta*, 1990, **177**, 115–120.
- 44 K. Zhang, A. A. Gonzalez and C. D. Hoff, *J. Am. Chem. Soc.*, 1989, **111**, 3627–3632.
- 45 A. A. Gonzalez, K. Zhang, S. P. Nolan, R. Lopez de la Vega, S. L. Mukerjee, C. D. Hoff and G. J. Kubas, *Organometallics*, 1988, **7**, 2429–2435.
- 46 D. E. Prokopchuk, E. S. Wiedner, E. D. Walter, C. V. Popescu, N. A. Piro, W. S. Kassel, R. M. Bullock and M. T. Mock, *J. Am. Chem. Soc.*, 2017, **139**, 9291–9301.
- 47 P. L. Holland, *Dalton Trans.*, 2010, **39**, 5415–5425.



- 48 C. Tsay and J. C. Peters, *Chem. Sci.*, 2012, **3**, 1313–1318.
- 49 J. L. Sudmeier, J. L. Evelhoch and N. B. H. Jonsson, *J. Magn. Reson.*, 1980, **40**, 377–390.
- 50 D. S. Stephenson and G. Binsch, *J. Magn. Reson.*, 1978, **32**, 145–152.
- 51 T. Le-Husebo and C. M. Jensen, *Inorg. Chem.*, 1993, **32**, 3797–3798.
- 52 D. C. Grills, R. van Eldik, J. T. Muckerman and E. Fujita, *J. Am. Chem. Soc.*, 2006, **128**, 15728–15741.
- 53 K. M. Gramigna, D. A. Dickie, B. M. Foxman and C. M. Thomas, *ACS Catal.*, 2019, **9**, 3153–3164.
- 54 W. H. Harman and J. C. Peters, *J. Am. Chem. Soc.*, 2012, **134**, 5080–5082.
- 55 R. C. Cammarota, L. J. Clouston and C. C. Lu, *Coord. Chem. Rev.*, 2017, **334**, 100–111.
- 56 S. Grimme, J. Antony, S. Ehrlich and H. Krieg, *J. Chem. Phys.*, 2010, **132**, 154104–154122.
- 57 Y. Zhao and D. G. Truhlar, *Theor. Chem. Acc.*, 2008, **120**, 215–241.
- 58 L. Zhao, M. von Hopffgarten, D. M. Andrada and G. Frenking, *Wiley Interdiscip. Rev.: Comput. Mol. Sci.*, 2018, **8**, e1345.
- 59 M. P. Mitoraj, A. Michalak and T. Ziegler, *J. Chem. Theory Comput.*, 2009, **5**, 962–975.
- 60 R. D. Shannon, *Acta Crystallogr., Sect. A: Cryst. Phys., Diffr., Theor. Gen. Crystallogr.*, 1976, **32**, 751–767.
- 61 M. V. Vollmer, J. Xie, R. C. Cammarota, V. G. Young, E. Bill, L. Gagliardi and C. C. Lu, *Angew. Chem., Int. Ed.*, 2018, **57**, 7815–7819.
- 62 D. D. Perrin, *Ionisation Constants of Inorganic Acids and Bases in Aqueous Solution*, Pergamon Press, Elmsford, NY, 2nd edn, 1982.
- 63 E. Y. Tsui, R. Tran, J. Yano and T. Agapie, *Nat. Chem.*, 2013, **5**, 293–299.
- 64 D. You and F. P. Gabbaï, *Trends in Chemistry*, 2019, DOI: 10.1016/j.trechm.2019.03.011.
- 65 A. Amgoune and D. Bourissou, *Chem. Commun.*, 2011, **47**, 859–871.
- 66 B. Cordero, V. Gómez, A. E. Platero-Prats, M. Revés, J. Echeverría, E. Cremades, F. Barragán and S. Alvarez, *Dalton Trans.*, 2008, **21**, 2832–2838.
- 67 J. Ye, R. C. Cammarota, J. Xie, M. V. Vollmer, D. G. Truhlar, C. J. Cramer, C. C. Lu and L. Gagliardi, *ACS Catal.*, 2018, **8**, 4955–4968.
- 68 P. A. Rudd, S. Liu, L. Gagliardi, V. G. Young and C. C. Lu, *J. Am. Chem. Soc.*, 2011, **133**, 20724–20727.
- 69 L. Krause, R. Herbst-Irmer, G. M. Sheldrick and D. Stalke, *J. Appl. Crystallogr.*, 2015, **48**, 3–10.
- 70 G. M. Sheldrick, *Acta Crystallogr., Sect. A: Found. Crystallogr.*, 2008, **64**, 112–122.
- 71 G. M. Sheldrick, *Acta Crystallogr., Sect. C: Struct. Chem.*, 2015, **71**, 3–8.
- 72 *Persistence of Vision (TM) Raytracer*, Persistence of Vision Pty. Ltd., Williamstown, Victoria, Australia, 2004.
- 73 Z.-L. Xue, A. J. Ramirez-Cuesta, C. M. Brown, S. Calder, H. Cao, B. C. Chakoumakos, L. L. Daemen, A. Huq, A. I. Kolesnikov, E. Mamontov, A. A. Podlesnyak and X. Wang, *Eur. J. Inorg. Chem.*, 2019, 1065–1089.
- 74 J. Zikovsky, P. F. Peterson, X. P. P. Wang, M. Frost and C. Hoffmann, *J. Appl. Crystallogr.*, 2011, **44**, 418–423.
- 75 A. J. Schultz, M. R. V. Jorgensen, X. Wang, R. L. Mikkelsen, D. J. Mikkelsen, V. E. Lynch, P. F. Peterson, M. L. Green and C. M. Hoffmann, *J. Appl. Crystallogr.*, 2014, **47**, 915–921.
- 76 A. J. Schultz, K. Srinivasan, R. G. Teller, J. M. Williams and C. M. Lukehart, *J. Am. Chem. Soc.*, 1984, **106**, 999–1003.
- 77 A. Thorn, B. Dittrich and G. M. Sheldrick, *Acta Crystallogr., Sect. A: Found. Crystallogr.*, 2012, **68**, 448–451.
- 78 C. R. Yonker and J. C. Linehan, *Prog. Nucl. Magn. Reson. Spectrosc.*, 2005, **47**, 95–109.
- 79 C. R. Yonker and J. C. Linehan, *J. Organomet. Chem.*, 2002, **650**, 249–257.
- 80 P. H. M. Budzelaar, *gNMR User Manual, 5.0*, IvorySoft, 2006.
- 81 M. J. Frisch, G. W. Trucks, H. B. Schlegel, G. E. Scuseria, M. A. Robb, J. R. Cheeseman, G. Scalmani, V. Barone, B. Mennucci, G. A. Petersson, *Gaussian 09, Revision E. 01*, Gaussian, Inc., Wallingford CT, 2009.
- 82 C. Adamo and V. Barone, *J. Chem. Phys.*, 1999, **110**, 6158–6170.
- 83 D. Andrae, U. Haeussermann, M. Dolg, H. Stoll and H. Preuss, *Theor. Chim. Acta*, 1990, **77**, 123–141.
- 84 F. Weigend and R. Ahlrichs, *Phys. Chem. Chem. Phys.*, 2005, **7**, 3297–3305.
- 85 A. V. Marenich, C. J. Cramer and D. G. Truhlar, *J. Phys. Chem. B*, 2009, **113**, 6378–6396.
- 86 *ADF2016, SCM, Theoretical Chemistry*, Vrije Universiteit, Amsterdam, The Netherlands, <http://www.scm.com>.
- 87 G. te Velde, F. M. Bickelhaupt, E. J. Baerends, C. Fonseca Guerra, S. J. A. van Gisbergen, J. G. Snijders and T. Ziegler, *J. Comput. Chem.*, 2001, **22**, 931–967.
- 88 E. Van Lenthe and E. J. Baerends, *J. Comput. Chem.*, 2003, **24**, 1142–1156.
- 89 E. Van Lenthe, J. Snijders and E. Baerends, *J. Chem. Phys.*, 1996, **105**, 6505–6516.
- 90 P. J. Hay and W. R. Wadt, *J. Chem. Phys.*, 1985, **82**, 299–310.
- 91 R. Krishnan, J. S. Binkley, R. Seeger and J. A. Pople, *J. Chem. Phys.*, 1980, **72**, 650–654.

